



# Evaluating present-day and future impacts of agricultural ammonia emissions on atmospheric chemistry and climate

Maureen Beaudor<sup>1,2</sup>, Didier Hauglustaine<sup>1</sup>, Juliette Lathière<sup>1</sup>, Martin Van Damme<sup>3,4</sup>, Lieven Clarisse<sup>3</sup>, and Nicolas Vuichard<sup>1</sup>

<sup>1</sup>Laboratoire des Sciences du Climat et de l'Environnement (LSCE) CEA-CNRS-UVSQ, Gif-sur-Yvette, France

<sup>2</sup>Now at : High Meadows Environmental Institute, Princeton University, Princeton, NJ 08544, USA

<sup>3</sup>Université libre de Bruxelles (ULB), Spectroscopy, Quantum Chemistry and Atmospheric Remote Sensing (SQUARES), Brussels, Belgium

<sup>4</sup>Royal Belgian Institute for Space Aeronomy, Brussels, Belgium

**Correspondence:** Maureen Beaudor (mb0142@princeton.edu)

**Abstract.** Agricultural practices are responsible for a major source of ammonia ( $\text{NH}_3$ ) to the atmosphere which has implications for air quality, climate and ecosystems. Due to the intensification of food and feed production, ammonia emissions are expected to increase significantly by 2100 and would therefore affect atmospheric composition such as nitrate ( $\text{NO}_3^-$ ) or sulfate ( $\text{SO}_4^{2-}$ ) particle formation and surface deposition feedback. Chemistry-climate models which integrate the key atmospheric physicochemical processes along with the ammonia cycle represent a useful tool to investigate present-day and also future ammonia pathways and their impact on the global scale. Ammonia sources are, however, challenging to quantify because of their dependencies on environmental variables and agricultural practices and represent a crucial input for chemistry-climate models. In this study, we use the chemistry-climate model LMDZ-INCA with agricultural and natural soil ammonia emissions from a global land surface model (ORCHIDEE with the integrated CAMEO module) for the present-day and 2090-2100 period under different socio-economic pathways. We show that this new set of emissions improves the spatial and temporal atmospheric ammonia representations in Africa, Latin America, and the US compared to the static reference inventory (CEDS). Higher ammonia emissions in Africa, as simulated by CAMEO compared to other studies, reflect enhanced present-day reduced nitrogen ( $\text{NH}_x$ ) deposition flux. This partially contributes to the 20% higher  $\text{NH}_x$  deposition in our results compared to other modeling studies at the global scale. Future CAMEO emissions lead to an overall increase of the global  $\text{NH}_3$  burden ranging from 37% to 70% while  $\text{NO}_3^-$  burden increases by 38% - 50% depending on the scenario even when global  $\text{NO}_x$  emissions decrease. When considering the most divergent scenarios (SSP5-8.5 and SSP4-3.4) for agricultural ammonia emissions the direct radiative forcing resulting from secondary inorganic aerosol changes ranges from -114 to -160  $\text{mW}\cdot\text{m}^{-2}$ . By combining a high level of  $\text{NH}_3$  emissions with decreased or contrasted future sulfate and nitrate emissions, the nitrate radiative effect can either overshoot (net total sulfate and nitrate effect of  $-200 \text{ mW}\cdot\text{m}^{-2}$ ) or be offset by the sulfate effect (net total sulfate and nitrate effect of  $+180 \text{ mW}\cdot\text{m}^{-2}$ ). We also show that future oxidation of  $\text{NH}_3$  could lead to an increase in  $\text{N}_2\text{O}$  emissions of 0.43 to 2.10  $\text{Tg}(\text{N}_2\text{O})_{\text{yr}^{-1}}$  compared to the present-day levels. Our results suggest that accounting for nitrate aerosol precursor emission levels but also for the ammonia oxidation pathway in future studies is particularly important to understand how ammonia will affect climate, air quality, and nitrogen deposition.



## 1 Introduction

25 Ammonia ( $\text{NH}_3$ ) is a key atmospheric species playing a crucial role in the alteration of air quality and climate through its  
implication in airborne particle matter formation (PM or aerosols) (Anderson et al., 2003; Bauer et al., 2007). The resulting  
aerosols, namely ammonium nitrates or ammonium sulfates, have important impacts on the Earth's radiative budget due to  
their ability to scatter the incoming radiation, act as cloud condensation nuclei, and indirectly increase cloud lifetime (Abbatt  
et al., 2006; Henze et al., 2012; Behera et al., 2013; Evangeliou et al., 2020). Through surface deposition processes,  $\text{NH}_3$  and  
30  $\text{NH}_4^+$  are also responsible for adverse damages to the ecosystems (Stevens et al., 2020; Guthrie et al., 2018; de Vries, 2021).

Agriculture and, more specifically, livestock manure management and land fertilization account for 85% of atmospheric  
 $\text{NH}_3$  (Behera et al., 2013). Because the volatilization of  $\text{NH}_3$  is highly dependent on temperature and humidity, land surface  
models (LSM) are promising to estimate  $\text{NH}_3$  emissions at the global scale. Recently, in Beaudor et al. (2023a), a specific  
LSM module dedicated to agricultural ammonia emissions (CAMEO, Calculation of AMmonia Emissions in ORCHIDEE) has  
35 been presented and evaluated against satellite-derived emission fluxes. CAMEO is a process-based model in which emissions  
from livestock management, grazing, and N fertilization (as well as natural soil sources) are interactively calculated within  
the ORCHIDEE Land Surface Model (ORganizing Carbon and Hydrology In Dynamic Ecosystems, Vuichard et al., 2019).  
CAMEO-based seasonal variation of  $\text{NH}_3$  emissions which depend on both meteorological and agricultural practices highlights  
a very good agreement with satellite-based emissions. In addition, the ability of CAMEO to simulate natural soil emissions  
40 is useful since they have been up to now poorly quantified at the global scale and appear a non-negligible source in specific  
regions such as Africa. Livestock activities and synthetic fertilizer use are projected to intensify in the following decades  
leading to a potential crucial  $\text{NH}_3$  emission increase. Impacts of the  $\text{NH}_3$  emissions on the future nitrate aerosol formations and  
climate have already been assessed in Hauglustaine et al. (2014) under Radiative Concentration Pathways (RCPs) scenarios  
until 2100 by using the global climate-chemistry atmospheric model LMDZ-INCA . They have illustrated the substantial  
45 impact of  $\text{NH}_3$  emissions on the future formation of nitrate aerosols and on the direct radiative forcing. By the year 2100,  
due to significant emissions from agriculture, the nitrate aerosol's contribution to anthropogenic aerosol optical depth could  
increase by as much as fivefold, under the most impactful scenario considered. RCP scenarios have also been exploited to  
study the importance of future atmospheric  $\text{NH}_3$  on chemistry and climate with a special focus on atmospheric  $\text{NH}_3$  removal  
treatments and oxidation processes (Paulot et al., 2016; Pai et al., 2021) Recently, in the CMIP6 exercise framework, socio-  
50 economical drivers have gained greater importance and have been incorporated in a new set of scenarios called SSPs (Shared  
Socioeconomic Pathways, SSPs) (O'Neill et al., 2016). The Sixth Assessment Report from the IPCC covers a broader range of  
greenhouse gas and air pollutant trajectories through the use of SSP scenarios (Intergovernmental Panel On Climate Change,  
2023). However, future agricultural  $\text{NH}_3$  emissions that have been prescribed for the Sixth Assessment Report have several  
limitations regarding the consideration of climate and livestock densities as described in Beaudor et al. (2024). Livestock  
55 distribution, which is considered an important driver of future  $\text{NH}_3$  emissions, has been recently projected up to 2100 following  
a unique downscaling method (Beaudor et al., 2024). In this latter study, CAMEO has been exploited to calculate future  $\text{NH}_3$   
emissions accounting for the evolution of climate, livestock, and N fertilizers.





By demonstrating encouraging results for the present-day, especially when compared to reference inventories, CAMEO emissions open promising perspectives to represent ammonia and related aerosols within chemistry-climate models. Like most chemistry-climate models, LMDZ-INCA relies on the seasonally-forced inventory called CEDS (Community Emissions Data System, McDuffie et al., 2020). We hypothesize that prescribing CAMEO emissions instead of CEDS for agricultural sources could improve the atmospheric species and aerosol concentrations as well as N deposition fluxes, especially over Africa, where important differences in the  $\text{NH}_3$  emissions have been demonstrated previously (Beaudor et al., 2023a). In the present paper, we introduce the impact of the new present-day and future CAMEO emission datasets on atmospheric chemistry by using the global LMDZ-INCA model. As a first global and regional evaluation, the columns simulated by LMDZ-INCA with CAMEO and CEDS inventories for the present-day have been compared to the  $\text{NH}_3$  columns observed by the IASI satellite instrument. Statistics involving ground-based measurements of surface concentrations ( $\text{NH}_3$ ,  $\text{NO}_2$ ,  $\text{NH}_4^+$ ,  $\text{NO}_3^-$ ,  $\text{SO}_4^{2-}$ ) have also been performed to ensure a more robust evaluation of the model. Emissions under SSP4-3.4 and SSP5-8.5 reflecting the most and least significant global increase by 2100 have been selected to assess the impact of future  $\text{NH}_3$  emissions on atmospheric chemistry. In addition, knowing the importance of sulfate dioxide ( $\text{SO}_2$ ) and nitrogen oxide ( $\text{NO}_x$ ) emissions in the nitrate and sulfate aerosol formation (Hauglustaine et al., 2014; Lachatre et al., 2019), scenarios have been designed to evaluate the impact of future  $\text{NH}_3$  emissions under contrasted  $\text{SO}_2$  and  $\text{NO}_x$  conditions. More precisely, in this paper, we present six simulations from LMDZ-INCA, including two present-day simulations, respectively with CEDS and CAMEO inventories for  $\text{NH}_3$  emissions and four future simulations over 2090-2100 with  $\text{NH}_3$  emissions from CAMEO and other sources at different levels. The structure of the paper is organized as follows: in Sect. 2, we present the emission inventories prepared and considered in the global chemistry-climate model for both the present-day and future (2100) simulations. In Sect. 3, we describe the LMDZ-INCA chemistry-climate model used along with modelling setup. Sect. 4 presents the simulated  $\text{NH}_3$  columns and the N deposition fluxes for the present-day including an evaluation of the model performance with IASI and ground-based measurements. In Sect.5 the perturbations associated with future agricultural emissions on atmospheric chemistry and climate under different scenarios are illustrated. Finally, in Sect. 6, we draw the conclusions from this work.

## 2 Emissions datasets

In this work, we focus on the impact of agricultural  $\text{NH}_3$  emissions calculated from CAMEO on atmospheric chemistry. Therefore, specific attention is given to the modelling of these emissions, which are further detailed in the two following sub-sections. Please note that at the exception of the agricultural and land-related  $\text{NH}_3$  emissions, all the other anthropogenic sources used in this study are based on the same sets of data (i.e. derived from the CMIP6 exercise both for present-day (CEDS) and future scenarios (McDuffie et al., 2020; Gidden et al., 2018)).

The global  $\text{NH}_3$ ,  $\text{NO}_x$  and  $\text{SO}_2$  emissions used in the study are presented in Table 1.



**Table 1.** Global ammonia ( $\text{NH}_3$ ), nitrogen ( $\text{NO}_x$ ) and sulfate ( $\text{SO}_2$ ) emissions used for the present-day (2004-2014) and future (2090-2100) simulations. Agricultural  $\text{NH}_3$  emissions are presented in parenthesis. ( $\text{TgNyr}^{-1}$  or  $\text{TgSyr}^{-1}$ ).

Simulation	$\text{NH}_3$	$\text{NO}_x$	$\text{SO}_2$
Present-day (2004-2014)			
CEDS	53 (38)	38	63
CAMEO	64 (35)	38	63
Future (2090-2100)			
CAMEO[585]	83 (50)	38	63
CAMEO[434]	97 (68)	38	63
CAMEO[434-126]	98 (68)	9.1	11
CAMEO[434-370]	104 (68)	38	46

## 2.1 Present-day agricultural $\text{NH}_3$ emissions

Two present-day agricultural  $\text{NH}_3$  emission datasets are tested. One simulation accounts for emissions from CEDS (McDuffie et al., 2020) and another one uses the estimated emissions from the CAMEO module included in the LSM ORCHIDEE described in Beaudor et al. (2023a). CAMEO simulates the manure production and agricultural  $\text{NH}_3$  emissions from the manure management chain (including manure storage and grazing) and soil emissions after fertilizer application. CAMEO simulates interactive  $\text{NH}_3$  emissions into the global LSM ORCHIDEE (Krinner et al., 2005; Vuichard et al., 2019). In addition, natural soil  $\text{NH}_3$  emissions are also accounted for in CAMEO. ORCHIDEE represents the C and N cycles and simulates the water and energy fluxes within the ecosystems. The vegetation is represented by 15 Plant Functional Type (PFTs) among which 2 crop types (C3 and C4) and 4 grass types (temperate, boreal and tropical C3 grasses and a single C4 grass). ORCHIDEE is constrained by land-use maps, meteorological fields, and N input such as synthetic fertilizers. Livestock densities represent one of the most critical input for CAMEO since it is the main driver of the feed need estimation and, thus, of indoor and, to a lesser extent, soil emissions.

Emissions from agriculture are slightly lower in CAMEO compared to CEDS (35 against 38  $\text{TgNyr}^{-1}$ ), but additional natural emissions from soil account for 13  $\text{TgNyr}^{-1}$ . As a result, global annual  $\text{NH}_3$  emissions from CAMEO are 10  $\text{TgNyr}^{-1}$  higher than in CEDS (Table. 1).

## 2.2 Future emission scenarios

In this study, future emissions for different SSPs are used for the 2090-2100 period. CAMEO emissions for SSP5-8.5 and SSP4-3.4 have been exploited for future agricultural and natural  $\text{NH}_3$  emissions in the CAMEO[SSPi] (SSPi: 585, 434, 434-126,



434-370) simulations where agricultural sources account for 50 and 68 TgNyr<sup>-1</sup> (respectively for SSP5-8.5 and SSP4-3.4). SSP5-8.5 and SSP4-3.4 have been chosen primarily as it represents, respectively, the least and most important increase of NH<sub>3</sub> emission estimated over 2090-2100 (Beaudor et al., 2024). These datasets have been recently constructed from a new gridded livestock product and future fertilizer input and evaluated against CMIP6 emissions in Beaudor et al. (2024). In addition to  
110 future CAMEO NH<sub>3</sub> emissions for SSP4-3.4, future CMIP6 emissions have been used for SSP1-2.6 and SSP3-7.0 (Gidden et al., 2018) for other emitted species but also for the anthropogenic sectors - other than agriculture - for NH<sub>3</sub> (waste, industry, etc). These two SSPs were selected because they represent divergent scenarios for global NO<sub>x</sub> and SO<sub>2</sub> emissions. SSP1-2.6 represents a "low" scenario with stringent emission regulations implemented almost worldwide. In contrast, SSP3-7.0 features contrasting emission trends, with strong regulations in the Northern Hemisphere and increasing emissions in the Southern  
115 Hemisphere. A slight difference in the NH<sub>3</sub> emissions is observable from CAMEO[434-126] and CAMEO[434-370] (Table 1). This difference is explained by the differences in the emissions from other anthropogenic sectors between SSP1.2-6 and SSP3-7.0. It is worth noticing that even though future total NO<sub>x</sub> emissions are similar between the present-day level and under SSP3-7.0 at the global scale, different regional patterns are observable (see Figure S1 in the Supplementary Material).

### 3 The LMDZ-INCA model

120 The LMDZ-INCA global chemistry–aerosol–climate model couples the LMDZ (Laboratoire de Météorologie Dynamique, version 6) general circulation model (GCM; Hourdin et al., 2020) and the INCA (INteraction with Chemistry and Aerosols, version 5) model (Hauglustaine et al., 2004, 2014). The interaction between the atmosphere and the continental surface is ensured through the coupling of LMDZ with the ORCHIDEE (version 1.9) dynamical vegetation model (Krinner et al., 2005). The present configuration is parameterized with the “Standard Physics” of the GCM (Boucher et al., 2020). The model incor-  
125 porates 39 hybrid vertical levels extending up to 70 km with a horizontal resolution of 1.3° in latitude and 2.5° in longitude. The GCM primitive equations are solved with a 3 min time step, large-scale transport of tracers is carried out every 15 min, and physical and chemical processes are calculated at a 30 min time interval.

The INCA model represents a state-of-art CH<sub>4</sub>-NO<sub>x</sub>-CO-NMHC-O<sub>3</sub> tropospheric photochemistry (Hauglustaine et al., 2004; Folberth et al., 2006). The tropospheric photochemistry and aerosol scheme includes a total of 123 tracers including 22  
130 tracers representing aerosols. The model represents 234 homogeneous chemical reactions, 43 photolytic, and 30 heterogeneous reactions. The tropospheric chemistry reactions are listed in Hauglustaine et al. (2004) and Folberth et al. (2006). Comparisons with observations have been extensively carried out to evaluate the gas-phase version of the model in the lower stratosphere and upper troposphere. The distribution of aerosols is represented by considering anthropogenic sources such as sulfates, nitrates, black carbon (BC), organic carbon (OC), as well as natural aerosols such as sea salt and dust. Reactions in the heterogeneous  
135 phase on both natural and anthropogenic tropospheric aerosols are also included (Bauer et al., 2004; Hauglustaine et al., 2004, 2014). A modal approach for the size distribution is used to track the number and mass of aerosols which is described by a superposition of five log-normal modes (Schulz, 2007).



The particle modes are represented for three ranges: sub-micronic (diameter  $<1 \mu\text{m}$ ) corresponding to the accumulation mode, micronic (diameter between 1 and  $10 \mu\text{m}$ ) corresponding to coarse particles, and super-micronic or super coarse particles (diameter  $>10 \mu\text{m}$ ). The diversity in chemical composition, hygroscopicity and mixing-state is ensured by distinguishing soluble and insoluble modes. Specifically, soluble and insoluble aerosols are treated separately in both sub-micron and micron modes. Sea salt,  $\text{SO}_4$ ,  $\text{NO}_3$ , and methane sulfonic acid (MSA) are treated as soluble components of the aerosol, dust is treated as insoluble, whereas BC and OC appear in both the soluble and insoluble fractions. Ammonia and nitrate aerosols are represented through an extended chemical scheme that includes the ammonia cycle as described by Hauglustaine et al. (2014). The formation of the ammonium sulfate aerosols depends on the relative ammonia and sulfate concentrations and is characterized by three chemical domains (ammonium-rich, sulfate-rich and sulfate-very rich conditions) as in Metzger et al. (2002). Extensive evaluations of the aerosol component of the LMDZ-INCA model have been carried out during the various phases of AEROCOM (e.g. Glib et al., 2021; Bian et al., 2017). Simulated surface  $\text{NH}_3$ ,  $\text{HNO}_3$ ,  $\text{NH}_4^+$ ,  $\text{SO}_4^{2-}$ ,  $\text{NO}_3^-$  concentrations indicate satisfying performances when evaluated against observation network from the US, Europe and Asia (Bian et al. 2017). The dry and wet deposition processes of ammonia, ammonium nitrate and ammonium sulfate are described in Hauglustaine et al. (2004) with updated Henry's law coefficients taken from Sander (2015). Coarse nitrates on dust and sea salt are deposited as the corresponding dust and sea-salt components.

### 3.1 Model setup

The model was run with meteorological data from the European Centre for Medium-Range Weather Forecasts (ECMWF) ERAInterim reanalysis. The GCM wind components are adjusted using the ECMWF meteorology and applying a correction term to the GCM u and v wind components at each time step with a relaxation time of 2.5 h (Hauglustaine et al., 2004). The ECMWF fields are provided every 6 hours and interpolated onto the LMDZ grid. We focus this work on the impact of agricultural  $\text{NH}_3$  emissions calculated from CAMEO on atmospheric composition and its future evolution. In order to isolate the impact of CAMEO  $\text{NH}_3$  emissions, all snapshot simulations are performed under present-day climate conditions and run for 11 years after a 2-year spin-up. Therefore, ECMWF meteorological data for 2004–2014 are used. The impact of climate change on agricultural  $\text{NH}_3$  emissions is however an interesting topic to be further investigated in the future.

Natural emissions are aggregated to anthropogenic sources in the INCA model. Biogenic surface fluxes of isoprene, terpenes, acetone, methanol are calculated offline within the ORCHIDEE vegetation model as described by Messina et al. (2016).  $\text{NH}_3$  emissions from ocean are taken from Bouwman et al. (1997) and reach  $8.2 \text{ TgNyr}^{-1}$  for the present-day. Natural emissions of dust and sea salt are computed using the 10 m wind components from the ECMWF reanalysis. For the future simulations (2090-2100), the SSP1-2.6 and SSP3-7.0 anthropogenic emissions (except agricultural sources) provided by Gidden et al. (2018) are used. Natural emissions (except natural soil  $\text{NH}_3$  emissions) and biomass burning for both gaseous species and particles are kept to their present-day level even in future simulations in order to isolate the impact of CAMEO emissions. In total, we performed six simulations, including two present-day simulations, respectively, with CEDS (1) and CAMEO (2) inventories for  $\text{NH}_3$  emissions and four future simulations over 2090-2100 with  $\text{NH}_3$  emissions from CAMEO under SSP5.8-5 and SSP4-3.4 by keeping other sources from the present-day levels (3 and 4), by taking the SSP1-2.6 (low levels; 5) and



SSP3-7.0 (contrasted conditions; 6) for other sources. Table 2 summarizes the simulations performed and analyzed in this study.

**Table 2.** Simulation set-up and corresponding emission datasets. The emission period used is given in parentheses. 'Other anth.' accounts for all the species for all the anthropogenic sectors except NH<sub>3</sub> emitted from the agricultural sector

Simulation name	Agri. NH <sub>3</sub> emissions	Other anth. emissions
Present-day (2004-2014)		
(1) CEDS	CEDS (2004-2014) <i>McDuffie et al. (2020)</i>	CEDS (2004-2014) <i>McDuffie et al. (2020)</i>
(2) CAMEO	CAMEO (2004-2014) <i>Beaudor et al. (2023a)</i>	CEDS (2004-2014) <i>McDuffie et al. (2020)</i>
Future (2090-2100)		
(3) CAMEO[585]	CAMEO SSP5-8.5 (2090-2100) <i>Beaudor et al. (2024)</i>	CEDS (2004-2014) <i>McDuffie et al. (2020)</i>
(4) CAMEO[434]	CAMEO SSP4-3.4 (2090-2100) <i>Beaudor et al. (2024)</i>	CEDS (2004-2014) <i>McDuffie et al. (2020)</i>
(5) CAMEO[434-126]	CAMEO SSP4-3.4 (2090-2100) <i>Beaudor et al. (2024)</i>	CEDS SSP1-2.6 (2090-2100) <i>Gidden et al. (2018)</i>
(6) CAMEO[434-370]	CAMEO SSP4-3.4 (2090-2100) <i>Beaudor et al. (2024)</i>	CEDS SSP3-7.0 (2090-2100) <i>Gidden et al. (2018)</i>

## 4 Present-day atmospheric ammonia, aerosol concentrations and nitrogen deposition fluxes

### 175 4.1 Global, regional and seasonal evaluation with IASI

For over a decade, the IASI instrument has provided measurements of NH<sub>3</sub> at a satisfying spatial resolution and large-scale coverage, which is convenient for modelling evaluation (Van Damme et al., 2014). The simulated monthly distributions of NH<sub>3</sub> are evaluated against observations over 2011-2014 from IASI at the global and regional scale. The IASI data used in this study originates from the IASI instruments onboard Metop-A and B, which were launched in 2006 and 2012 respectively. Each instrument overpasses the Earth two times per day with a footprint of 12 km at the nadir. The instruments cross the equator in the morning at 9:30 am and evening at 9:30 pm. Here we used the IASI NH<sub>3</sub> columns retrieved with version 3 of the "Artificial Neural Network for IASI (ANNI)" algorithm. An extended description of the retrieval methods and validation works can be found in various publications (Whitburn et al., 2016; Van Damme et al., 2017, 2021; Guo et al., 2021). In the present study, only the morning overpasses have been used as infrared instruments are more sensitive to the lowest layers of the atmosphere at this time of the day (Clarisse et al., 2010). Considering the daily cycle of NH<sub>3</sub> and to be consistent with the satellite observations, the model was run at a 30-min time-step, and sampled at the corresponding satellite overpass time. Regarding the spatial resolution, the IASI dataset has been gridded on the LMDZ-INCA grid (i.e. resolution of 1.3° in latitude and 2.5°



in longitude). The evaluation consists of comparisons of the spatial total  $\text{NH}_3$  columns for the two present-day runs (CEDS and CAMEO) along with a seasonal cycle analysis over the hot-spot regions. Taylor plots and Mean Bias Errors scores (MBE; mean of the difference between the observation and model) are also presented to assess the spatial and temporal variability of the simulated concentrations compared to the IASI observations considered as the reference. While IASI observations have already been used for CTM evaluations (Heald et al., 2012; Ge et al., 2020; Wang et al., 2021; Vira et al., 2022; Ren et al., 2023), this is the first time that simulated  $\text{NH}_3$  columns from LMDZ-INCA are evaluated against spaceborne observations. The Taylor plot approach aims at representing multiple statistical metrics including the normalized standard deviation, the Pearson's R correlation and a skill function which help at discriminating the best simulation. The default skill function implemented is defined in Taylor (2001) and decreases toward zero as the correlation becomes more and more negative or as the standard deviation approaches either zero or infinity.

The distributions of the  $\text{NH}_3$  columns observed by IASI and computed by LMDZ-INCA with the CEDS or CAMEO  $\text{NH}_3$  emissions over 2011-2014 are shown in Figure 1. The CAMEO simulation captures the  $\text{NH}_3$  hotspots over India, Equatorial Africa, Latin America, and the US where the columns are in the range 1 - 6 molecules  $\times 10^{16}\text{cm}^{-2}$ . When the CEDS inventory is replaced by CAMEO in LMDZ-INCA, the simulated columns are globally higher (of around 0.04 molecules  $\times 10^{16}\text{cm}^{-2}$ ) and the biggest differences are located in Northwestern India where the CAMEO columns are higher by about 2 molecules  $\times 10^{16}\text{cm}^{-2}$ . CAMEO emissions are also enhancing  $\text{NH}_3$  columns in China, Latin America, the US, and Africa, especially in the Equatorial region when compared to the CEDS simulation. Using CAMEO emissions improved the agreement of LMDZ-INCA with IASI observations in these regions. In particular, the Mean Bias Error (MBE) of the model is reduced from more than 50 % of the observed IASI columns in Equatorial Africa and South America when using CAMEO emissions instead of CEDS inventory (Table 3). The Taylor plots in Figure 2 highlight the better performance of the simulated spatial representation of the  $\text{NH}_3$  columns in these two regions when CAMEO emissions are prescribed. However, it is important to note potential compensating errors within the regions, particularly in Africa. In the Saharan region, CAMEO emissions lead to an overestimation of the columns (0.3 molecules  $\times 10^{16}\text{cm}^{-2}$ ), while in the tropical Sub-Saharan region, CAMEO emissions still result in an underestimation of the columns (- 0.4 molecules  $\times 10^{16}\text{cm}^{-2}$ ), potentially due to inaccuracies in the biomass burning inventory. Over the US, the modeled bias is also significantly reduced when using CAMEO emissions (47 %). It is partially explained by a closer standard deviation to the observations (normalized standard deviation around 1); however, CEDS simulation seems to be slightly more correlated to IASI (Figure 2).

On the Western coast of Africa, the CAMEO emissions also lead to an improvement where the resulting columns over the Atlantic Ocean depict the same pattern as IASI. It is explained by higher agricultural emissions and the addition of natural soil emissions calculated by CAMEO, which are missing in CEDS (see Figure S1 in the Supplementary Material). In India, both model simulations result in a normalized standard deviation close to 1 for the spatial distributions. The correlations are high ( $|r| > 0.8$ ), but the spatial patterns correlate better with IASI when using CAMEO. Over India, even though the bias is slightly reduced in CAMEO, the model overestimates the columns with a remaining high bias ( $\sim -0.18$  molecules  $\times 10^{16}\text{cm}^{-2}$ ).

The mean seasonal cycle over 2011-2014 is also analyzed for several regions (Figure 3). The seasonal cycle of the two simulated  $\text{NH}_3$  columns correlates with the emission's temporal evolution (not shown). The seasonal variations of  $\text{NH}_3$  column



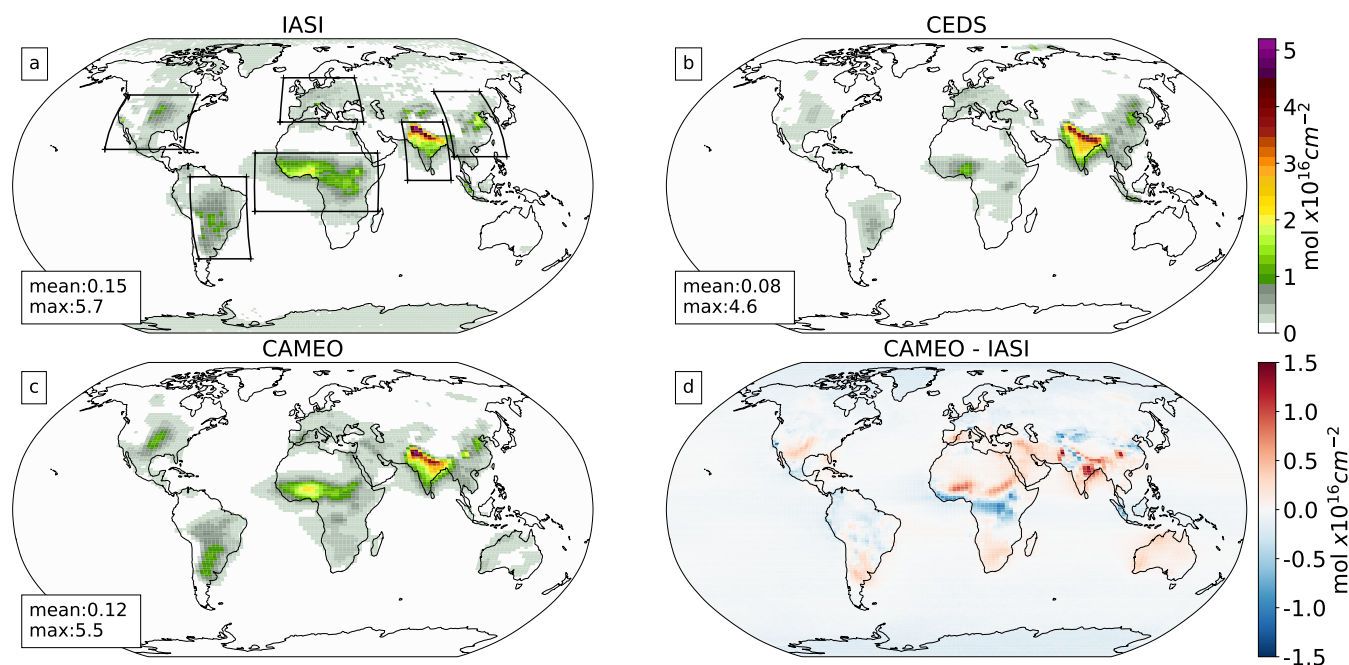


**Figure 1.** Mean annual  $\text{NH}_3$  atmospheric columns observed by the IASI instrument (a) and calculated in the CEDS (b) and CAMEO (c) simulations (2011-2014). The absolute anomalies between the CAMEO and IASI columns are shown in (d). The black boxes in (a) delimit the regional bounds used in the statistical analysis in the Taylor plots (Figure 2), the time-series analysis (Figure 3) and in the Mean Bias Error calculation in Table 3. ( $\text{molecules} \times 10^{16} \text{cm}^{-2}$ ).

**Table 3.** Regional spatial Mean Bias Error (MBE)  $\text{NH}_3$  columns from CEDS and CAMEO simulation ( $\text{molecules} \times 10^{16} \text{cm}^{-2}$ ). The biases are computed by using IASI observations over the 2011-2014 period. The numbers of pixels within the regions over which the average has been computed are given in parenthesis for each region

Region (# pixels)	Mean Obs.	MBE CEDS	MBE CAMEO
Eq. Africa (775)	0.51	0.30	0.05
China (360)	0.31	-0.06	-0.01
Europe (418)	0.21	0.01	0.003
India (286)	0.83	-0.23	-0.18
S. America (504)	0.37	0.21	-0.0007
US (460)	0.28	0.13	-0.001

in the CEDS simulation highlight two peaks in April and September for most regions reflecting the artificial seasonal profile used in the inventory. In CAMEO, the seasonality varies according to the region. In the US and Europe, there is a unique peak

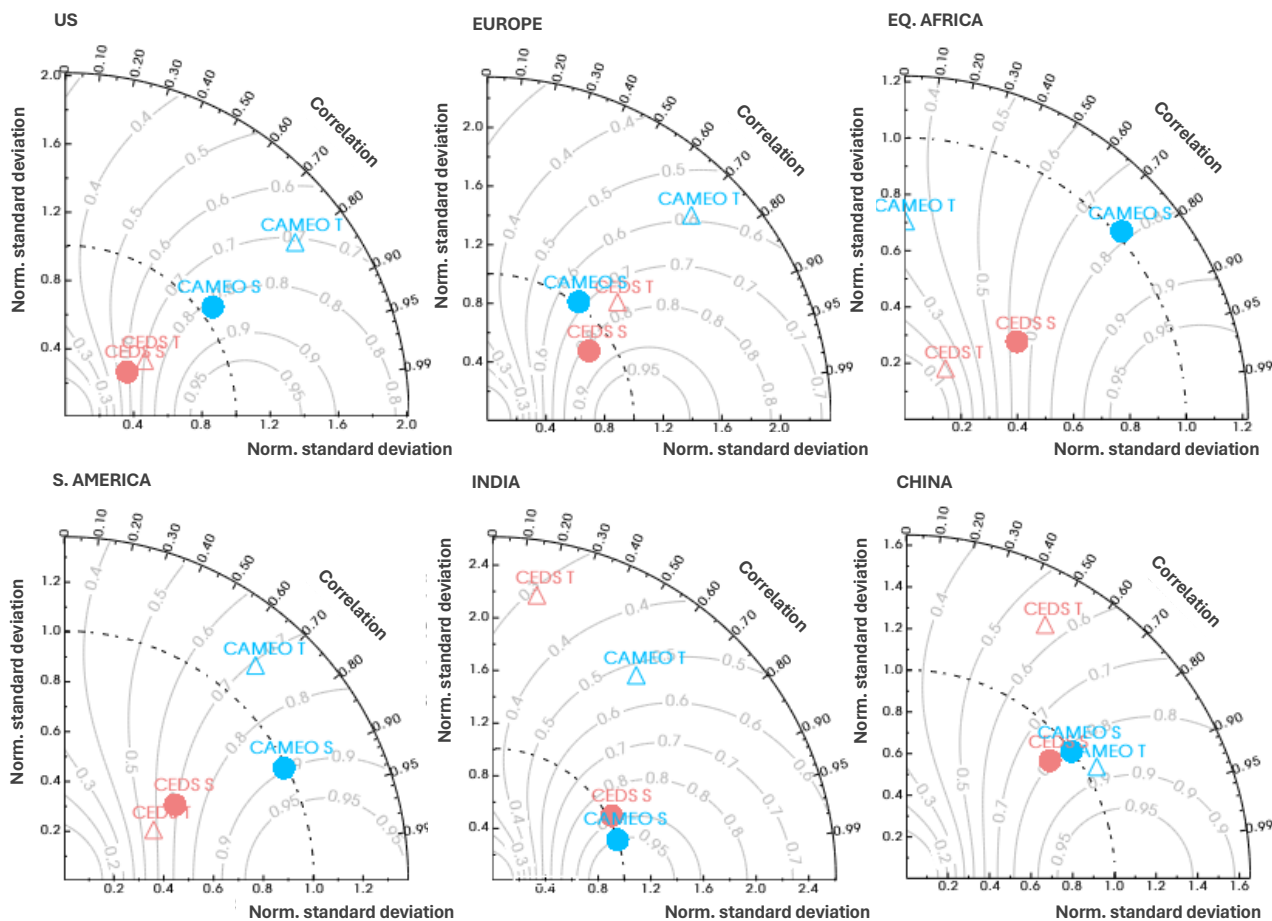


**Figure 2.** Regional Taylor plots for the simulated atmospheric  $\text{NH}_3$  columns from the CAMEO and CEDS simulations evaluated with IASI observations. The plots include temporal at the monthly time step (first averaged in space over the corresponding regions, triangle markers, and T labels) and spatial (first averaged in time over monthly time-series of the 2011-2014 period, plain circles markers, and S labels) statistic metrics, including the normalized standard deviation (presented on the x-y axis, observation = 1), the Pearson's R correlation and a skill function (grey isolines). It is important to note that each region has been chosen carefully with a sufficient number of pixels as given in Table 3. The plots have been performed by using the CDAT library in Python according to Taylor (2001).

225  $(0.7 \text{ molecules} \times 10^{16} \text{ cm}^{-2})$  during summer which is not revealed in the IASI observations where there is rather a maximum  
 value  $(0.5 \text{ and } 0.4 \text{ molecules} \times 10^{16} \text{ cm}^{-2}, \text{ respectively})$  reached over several months (March-September). Over Equatorial  
 Africa, South America, India, and China, CAMEO shows a good agreement with IASI columns and the seasonal cycles  
 are very close, with values of the same ranges. CAMEO emissions improve the representation of the atmospheric columns,  
 especially in South America and Equatorial Africa, where the columns in CEDS are at least 2 times lower compared to IASI. In  
 230 Africa, the temporal variability is more accurately simulated with CAMEO with a higher skill function in the Taylor plot, even



though the correlation is reduced (Figure 2). Over South America, the improvement is even stronger where the skill function gained 2 units. In India, the peak value is much higher ( $\sim 1.5 \text{ molecules} \times 10^{16} \text{ cm}^{-2}$ ) and occurs earlier with CEDS (May) than with IASI and CAMEO. CAMEO depicts a better seasonal amplitude with a 2- month peak starting in May and lasting until June, closer to the observations leading to a better model performance (Figure 2).

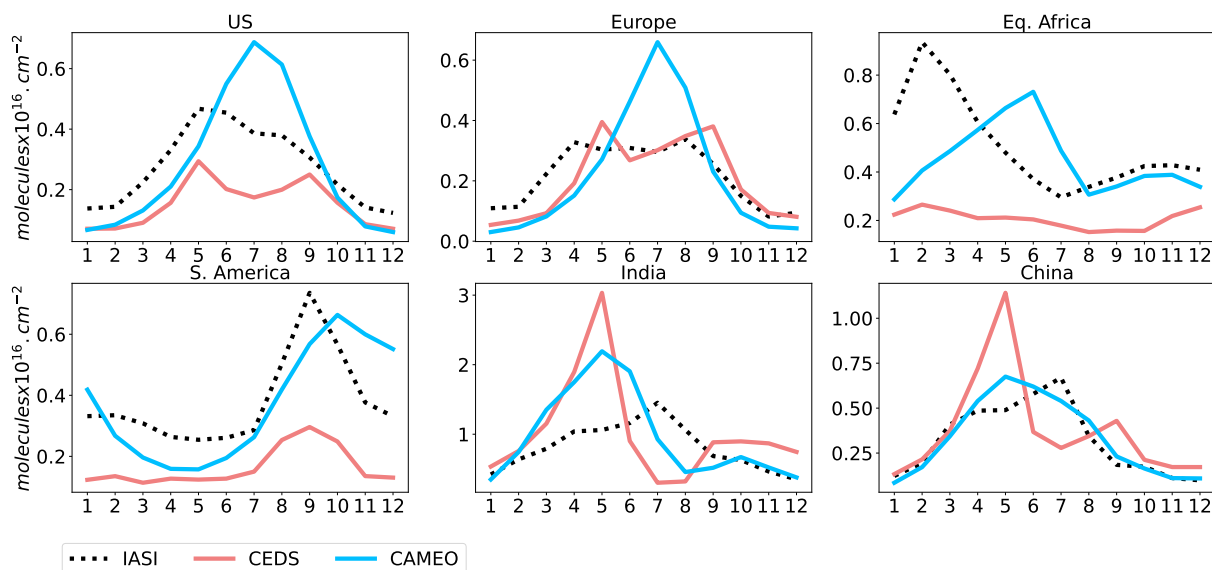


**Figure 3.** Regional mean seasonal cycle (2011-2014) of  $\text{NH}_3$  atmospheric columns observed by the IASI satellite (black dotted lines) and calculated in the CEDS (pink lines) and CAMEO (blue lines) simulations ( $\text{molecules} \times 10^{16} \text{ cm}^{-2}$ ).

235 The evaluation of the  $\text{NH}_3$  columns highlights a global improvement of the spatial and temporal patterns when using CAMEO emissions compared to CEDS, especially regarding the seasonal cycle where the skill functions denoted in the Taylor plots are much higher when comparing the temporal variability of both simulations to the IASI observations. It is important to note that in Africa, even though CAMEO emission prescription seems promising to improve the seasonal cycle of the columns, biomass burning emissions play a key role in the temporal representation, which can leave room for further improvements. In  
 240 this specific region, IASI-derived AOD in the thermal infrared have revealed important dust events (10 to 20 % of days with AOD larger than 0.2 ; Lachatre et al., 2020).

#### 4.2 Regional comparison with worldwide ground-based networks

Ten monitoring networks of surface  $\text{NH}_3$ ,  $\text{NH}_4^+$ ,  $\text{NO}_2$ ,  $\text{NO}_3^-$  and  $\text{SO}_4^{2-}$  concentrations from East Asia, North America and Europe have been exploited to extend our evaluation beyond the  $\text{NH}_3$  columns. Simulated surface concentrations have  
 245 been compared on a yearly basis to data observed from 2015 by extracting for each site the closest pixel from the LMDZ-



INCA simulation. As recommended in Ge et al. (2021), we only consider measurements where 75% of the year was captured in order to avoid bias in our analysis. In this study, we utilize data from the Chinese National Nitrogen Deposition Monitoring Network (NNDMN from Xu et al., 2019), the acid deposition monitoring network in East Asia and Southeast Asia (EANET, 13 countries, <https://www.eanet.asia/>), the UK Acid Gases and Aerosol Monitoring Network (AGANet, 30 sites, <https://uk-air.defra.gov.uk/networks/network-info?view=aganet>), the European Monitoring and Evaluation Programme/Chemical Coordinating Centre (EMEP/CCC, <https://ebas-data.nilu.no/default.aspx>), the United States Environmental Protection Agency (EPA, <https://www.epa.gov/outdoor-air-quality-data>), the Ammonia Monitoring Network (AMoN, <https://nadp.slh.wisc.edu/sites/amon-ab35/>) and the National Air Pollution Surveillance (NAPS, <https://www.canada.ca/en/services/environment/weather/airquality.html>) program. Main statistic scores are given in Table 4 comparing observations with both CAMEO and CEDS runs. Scatter plots of annual mean modelled in CAMEO and measured surface concentrations along with Pearson's coefficients are given for each regional network in Figure 4, 5 and 6. Analog plots for the CEDS simulation are given in the Supplementary Material (Fig. S4, S5 and S6). Overall surface  $\text{NH}_3$ ,  $\text{NH}_4^+$ ,  $\text{NO}_2$ ,  $\text{NO}_3^-$  and  $\text{SO}_4^{2-}$  concentrations simulated by LMDZ-INCA are well correlated to the observations worldwide ( $R_T > 0.5$ ). Simulated concentrations are however underestimated for most species, especially in China where the observed concentrations are by far the highest with for instance an estimated MBE for  $\text{NH}_3$  concentrations at  $6.0 \mu\text{g}\cdot\text{m}^{-3}$  (annual observed average at  $10.4 \mu\text{g}\cdot\text{m}^{-3}$ , Table 4). This positive bias seems to be due to an underestimation in the hotspot region of Beijing but also in more remote areas where differences can reach  $16.2 \mu\text{g}\cdot\text{m}^{-3}$  (Figure 4). The IASI instrument does not necessarily detect the highest columns in these regions (Figure 1). For most networks, prescribing CAMEO highlights reductions in bias compared to CEDS (-38% for US EPA and -18 % for EMEP/CCCC). In North America, CAMEO reflects a realistic spatial pattern against measurements with high concentrations localized in the Mid-US ( $> 4 \mu\text{g}\cdot\text{m}^{-3}$ ) and rather low concentrations at the Mid-Atlantic side. An underestimation from CAMEO is still observable in the Mid-West region ( $< 2 \mu\text{g}\cdot\text{m}^{-3}$ ). CAMEO emissions do not improve the  $\text{NH}_3$  concentration representations measured in the EANET and UK networks.

### 4.3 Surface nitrogen deposition intercomparison

In this section, we present an analysis of the total (dry plus wet) annual deposition of  $\text{NH}_x$  ( $= \text{NH}_3 + \text{NH}_4^+$ ), and  $\text{NO}_y$  ( $= \text{NO} + \text{NO}_2 + \text{NO}_3 + \text{HNO}_2 + \text{HNO}_3 + \text{HNO}_4 + 2 \text{N}_2\text{O}_5 + \text{PAN} + \text{organic nitrates} + \text{particulate NO}_3^-$ ).

The simulated deposition fluxes (CEDS and CAMEO) are also compared against two model-based estimates, one used in the most recent CMIP exercise (IGAC/SPARC Chemistry–Climate Model Initiative (CCMI; Eyring et al., 2013 hereafter)) and the other using EMEP MSC-W (European Monitoring and Evaluation Programme Meteorological Synthesizing Centre –West) from Ge et al. (2022). N depositions fluxes from CCMI are commonly used as forcing files in LSM, as in the ORCHIDEE model. CCMI deposition fields are available globally at a resolution of  $0.5 \times 0.5$  degrees from 1860 to 2014. In the CCMI models, nitrogen emissions from natural biogenic sources, lightning, anthropogenic sources, and biomass burning are taken from CMIP5 exercise (Lamarque et al., 2010). Regarding N deposition from Ge et al. (2022), the CTM EMEP MSC-W has been used to simulate dry and wet deposition fluxes of  $\text{N}_r$  species for 2015. In their configuration, meteorology comes from the Weather Research and Forecast model (WRF, Simpson et al., 2012). The N anthropogenic emissions used were derived



**Table 4.** Summary statistics of model comparison (CAMEO and CEDS runs) with measurements for 2015 in East Asia and Southeast Asia (NNDMN and EANET networks), Europe and UK (EMEP/CCC, UK networks), North America (US, EPA, and NAPS). *N* represents the number of measuring sites. Annual average concentrations and Mean Bias Error (MBE) are given in  $\mu\text{g}\cdot\text{m}^{-3}$ .

Species	Region-Network	<i>N</i>	Mean Obs.	Mean CAMEO	Mean CEDS	MBE CAMEO	MBE CEDS
$\text{NH}_3$	NNDMN	25	10.4	4.32	3.52	6.06	6.86
	EANET	27	1.60	0.96	1.41	0.64	0.19
	EMEP/CCC	38	0.92	0.93	1.10	-0.02	-0.19
	UK networks	22	1.52	0.40	0.76	1.12	0.76
	US EPA	31	1.22	0.95	0.59	0.27	0.63
	NAPS	7	1.41	0.55	0.43	0.86	0.98
$\text{NH}_4^+$	NNDMN	24	8.09	2.13	1.89	6.0	6.20
	EANET	28	0.76	0.20	0.25	0.56	0.51
	EMEP/CCC	49	0.60	0.19	0.23	0.40	0.37
	UK networks	16	0.40	0.15	0.22	0.25	0.18
	US EPA	79	0.50	0.23	0.20	0.27	0.30
	NAPS	13	0.31	0.18	0.14	0.12	0.16
$\text{NO}_2$	NNDMN	25	24.1	19.5	18.66	4.56	5.39
	EANET	7	15.6	12.6	12.33	2.99	3.24
	EMEP/CCC	72	4.7	5.9	4.92	-1.21	-0.21
	UK networks	-	-	-	-	-	-
	US EPA	124	13.12	4.36	4.05	8.76	9.07
	NAPS	58	10.06	2.79	2.67	7.28	7.40
$\text{NO}_3^-$	NNDMN	25	10.20	4.66	4.27	5.54	5.93
	EANET	29	1.26	0.14	0.28	1.11	0.98
	EMEP/CCC	50	1.12	0.22	0.38	0.89	0.74
	UK networks	15	0.91	0.15	0.39	0.76	0.52
	US EPA	152	0.60	0.23	0.22	0.37	0.38
	NAPS	13	0.38	0.24	0.18	0.14	0.20
$\text{SO}_4^{2-}$	NNDMN	-	-	-	-	-	-
	EANET	29	3.27	0.85	0.77	2.42	2.50
	EMEP/CCC	48	1.26	0.48	0.40	0.78	0.86
	UK networks	17	0.45	0.43	0.36	0.03	0.10
	US EPA	155	1.00	0.44	0.39	0.56	0.61
	NAPS	13	0.82	0.54	0.44	0.27	0.38

280 from the V6 ECLIPSE inventory (<https://iiasa.ac.at/web/home/research/researchPrograms/air/ECLIPSEv6.html>) for 2015 with monthly profiles deduced from the EDGAR time series (Crippa et al., 2020) according to Ge et al. (2021).  $\text{NO}_x$  and VOC emissions from the forest, vegetation fires, lightning, and soil were also included.

As CCMI fluxes are only available until 2014 and files from Ge et al. (2022) are provided for 2015 only, a 2010-2014 climatology has been calculated for CCMI, CAMEO and CEDS simulated N depositions. Ge et al. (2022) do not provide

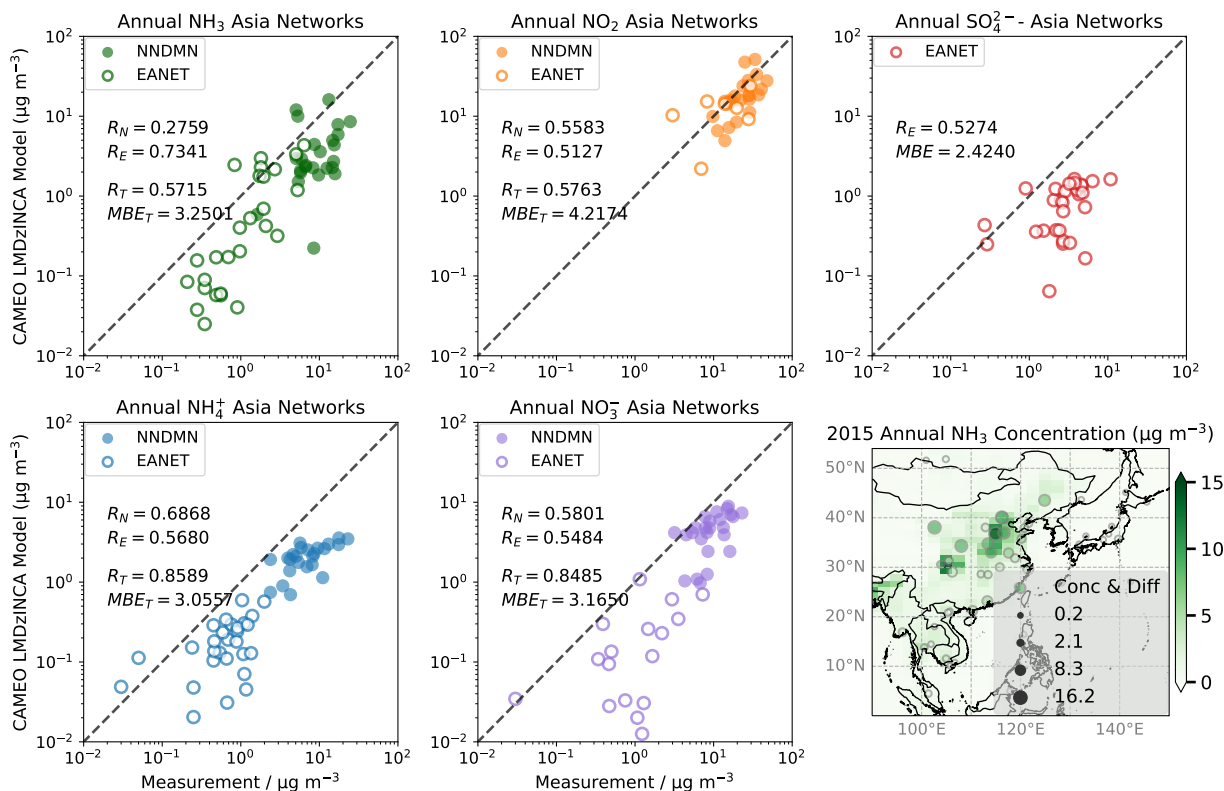


**Figure 4.** Scatter plots of annual mean modelled (CAMEO run) and measured  $\text{NH}_3$ ,  $\text{NO}_2$ ,  $\text{SO}_4^{2-}$ ,  $\text{NH}_4^+$  and  $\text{NO}_3^-$  concentrations at East Asian and Southeast Asian monitoring network locations for 2015. In each plot, the dashed black line is the 1 : 1 line.  $R_N$  is for NNDMN network.  $R_E$  is for the EANET network.  $R_T$  is the overall correlation coefficient between the model and all measurements shown.  $\text{MBE}_T$  is the overall Mean Bias Error between the model and all measurements shown. Note the log scale used in the plot. Annual surface  $\text{NH}_3$  simulated concentrations are also shown along with the observation values mapped with circles. The size of the circle indicates the absolute difference with the modelled value. ( $\mu\text{g}\cdot\text{m}^{-3}$ ).

285 monthly fields; thus, only CCMI, CAMEO and CEDS time series for the same 2010-2014 climatology have been further explored for the seasonality analysis.

Global  $\text{Nr}$  deposition was estimated at 108 and 127  $\text{TgN}\cdot\text{yr}^{-1}$  over 2010-2014 in the CEDS and CAMEO simulations (land, ~80 %; ocean, ~20 %). CEDS compares well with the 102 and 114  $\text{TgN}\cdot\text{yr}^{-1}$  estimated from CCMI and Ge et al. (2022) but CAMEO is closer to the 119  $\text{TgN}\cdot\text{yr}^{-1}$  quantified for 2010 from the recent study from Liu et al. (2022). The ratio of  $\text{NH}_x$  to total  $\text{Nr}$  depositions between CCMI, CEDS, and CAMEO show a good agreement, however, EMEP MSC-W depicts a much less important contribution of  $\text{NH}_x$  to the total  $\text{Nr}$  depositions all over the world.

290



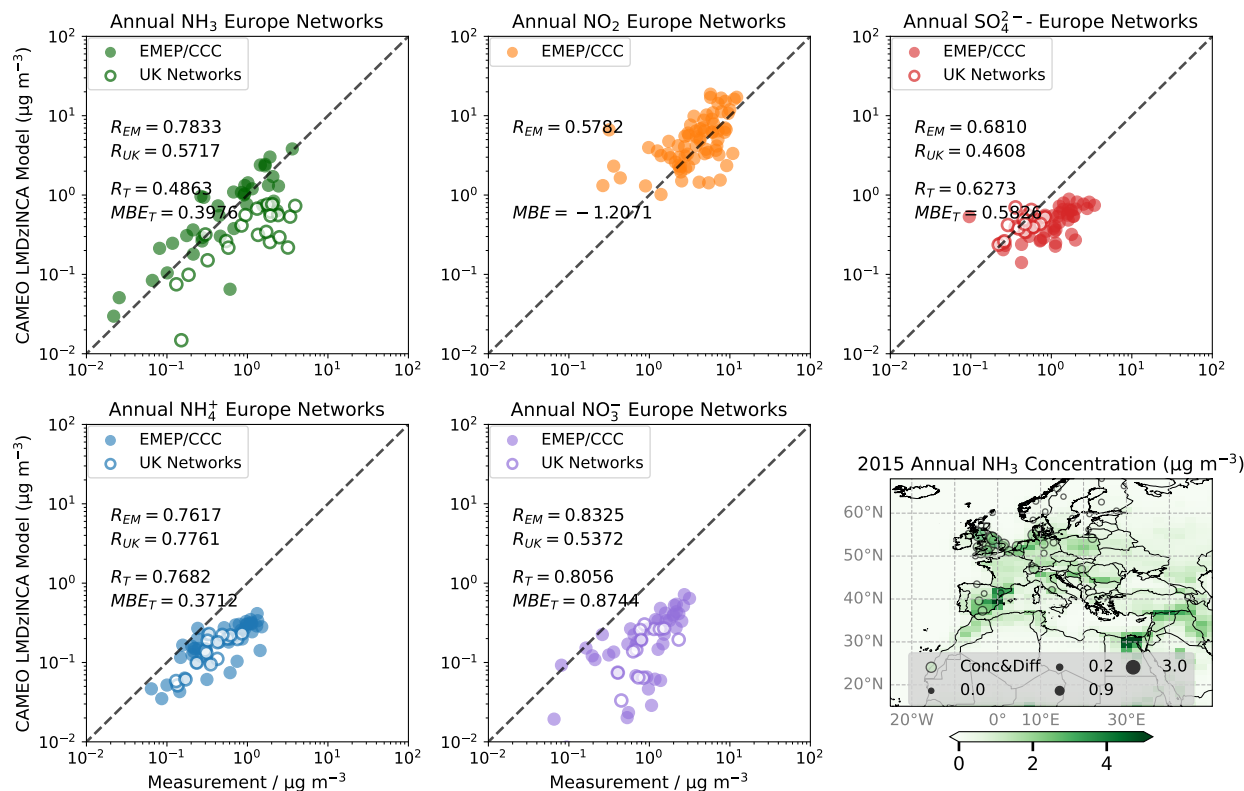


**Figure 5.** Scatter plots of annual mean modelled (CAMEO run) and measured  $\text{NH}_3$ ,  $\text{NO}_2$ ,  $\text{SO}_4^{2-}$ ,  $\text{NH}_4^+$  and  $\text{NO}_3^-$  concentrations at European and UK monitoring network locations for 2015. In each plot, the dashed black line is the 1 : 1 line.  $R_{EM}$  is for EMEP/CCC network.  $R_{UK}$  is for the UK network.  $R_T$  is the overall correlation coefficient between the model and all measurements shown.  $MBE_T$  is the overall Mean Bias Error between the model and all measurements shown. Note the log scale used in the plot. Annual surface  $\text{NH}_3$  simulated concentrations are also shown along with the observation values mapped with circles. The size of the circle indicates the absolute difference with the modelled value. ( $\mu\text{g}\cdot\text{m}^{-3}$ ).

### 4.3.1 Reduced Nitrogen Deposition

Global surface  $\text{NH}_x$  depositions reach  $65 \text{ TgN}\cdot\text{yr}^{-1}$  with CAMEO showing a good agreement between CCMI, CEDS and EMEP MSC-W and CAMEO appearing as the highest estimate (Figure 7). This difference between CAMEO and the other estimates is partly explained by the high values over Africa (Figure 8) with a total budget of  $14 \text{ TgN}\cdot\text{yr}^{-1}$  which is twice the one estimated in CCMI, CEDS and EMEP MSC-W but also to a smaller extent by higher budgets in Oceania and Latin America. Higher  $[\text{NH}_3]$  due to enhanced  $\text{NH}_3$  emissions in CAMEO explain these regional patterns together with no enhanced aerosol ( $\text{NH}_4^+$ ,  $\text{NO}_3^-$ ,  $\text{SO}_4^{2-}$ ) formation because of low  $\text{NO}_x$  conditions (Figure 9 and 10). It means that even though there is more  $\text{NH}_3$ , it remains in its gaseous phase and the deposition pathway is favored in these regions when CAMEO emissions are used. As mentioned previously, Vira et al. (2019) also estimated high agricultural  $\text{NH}_3$  emissions over Africa with the FAN

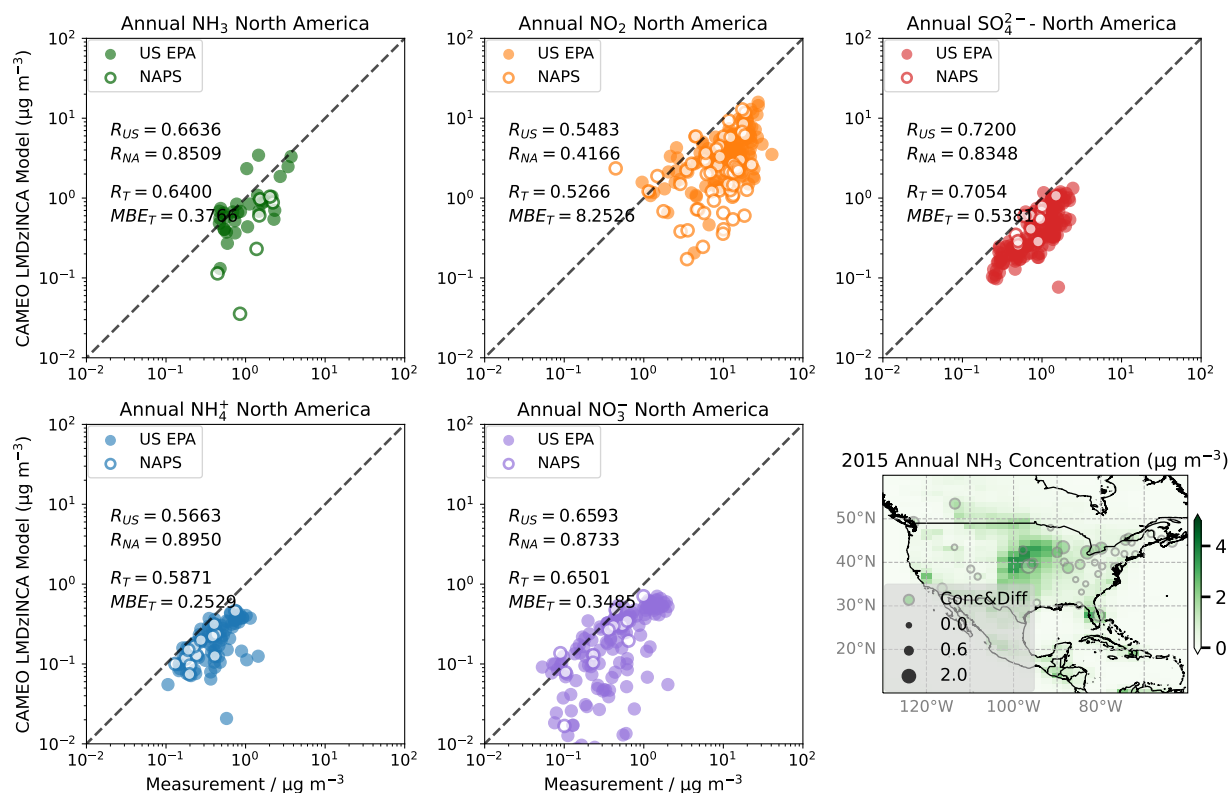


**Figure 6.** Scatter plots of annual mean modelled (CAMEO run) and measured  $NH_3$ ,  $NO_2$ ,  $SO_4^{2-}$ ,  $NH_4^+$  and  $NO_3^-$  concentrations at European and UK monitoring network locations for 2015. In each plot, the dashed black line is the 1 : 1 line.  $R_{US}$  is for the US/EPA network.  $R_{NA}$  is for the NAPS network.  $R_T$  is the overall correlation coefficient between the model and all measurements shown.  $MBE_T$  is the overall Mean Bias Error between the model and all measurements shown. Note the log scale used in the plot. Annual surface  $NH_3$  simulated concentrations are also shown along with the observation values mapped with circles. The size of the circle indicates the absolute difference with the modelled value. ( $\mu g \cdot m^{-3}$ ).

v2 model when compared to the literature. In a recent evaluation work using observations from the INDAAF network, they show an overestimation of their  $NH_x$  wet deposition flux of around 10 % (Vira et al., 2022). We also compared our simulated  $NH_x$  wet deposition fluxes from two grid cells corresponding to stations from the INDAAF network situated in western Africa (see Figure S5 in the Supplementary Material for the exact locations). CAMEO simulation compares much better than CEDS to the observed  $NH_4^+$  wet deposition, especially at the Katibougou station where a clear seasonal cycle with a similar peak in summer is represented (see Figure S6 in the Supplementary Material).

Regarding the other regions,  $NH_x$  depositions from LMDZ-INCA (both CEDS and CAMEO) and EMEP MSC-W reach values up to  $3000 \text{ mgN} \cdot \text{m}^{-2} \cdot \text{yr}^{-1}$  in India and China while CCMI fluxes do not exceed  $1900 \text{ mgN} \cdot \text{m}^{-2} \cdot \text{yr}^{-1}$  (Figure 8). Same patterns are observable over central Africa, Latin America, and the US where CCMI  $NH_x$  depositions (maximum between 500

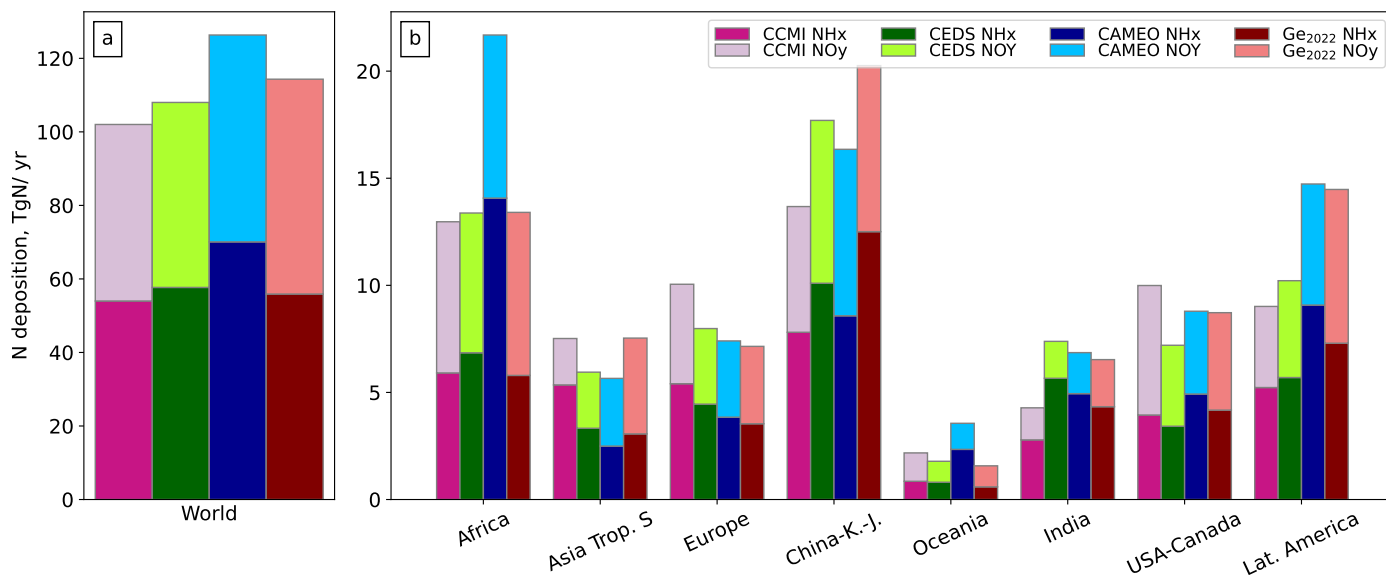


**Figure 7.** Global and regional annual NH<sub>x</sub> and NO<sub>y</sub> deposition in TgN.yr<sup>-1</sup> from CCMi for 2010-2014, CEDS and CAMEO simulations for 2010-2014 and by EMEP MSC-W (Ge et al., 2022) for 2015. Note that the global budget account for continents and oceans. China-K-J account for China-Korea-Japan

310 and 1000 mgN.m<sup>-2</sup>.yr<sup>-1</sup>) are lower than LMDZ-INCA and EMEP MSC-W deposition rates (maximum between 800 and 1900 mgN.m<sup>-2</sup>.yr<sup>-1</sup>). Over these regions, CAMEO simulation depicts much higher deposition fluxes which is explained by higher emissions prescribed in this run than in CEDS (see Figure S1 in the Supplementary Material). However, in south-eastern Asia CCMi deposition reach 7000 mgN.m<sup>-2</sup>.yr<sup>-1</sup> while in LMDZ-INCA and EMEP MSC-W maximum value is around 1400 mgN.m<sup>-2</sup>.yr<sup>-1</sup>.

315 There are important disagreements in the NH<sub>x</sub> deposition seasonal cycle between LMDZ-INCA simulations and CCMi in almost all the regions (see Figure S7 in the Supplementary Material). CEDS NH<sub>x</sub> depositions variations are well correlated with the NH<sub>3</sub> variations of the CEDS emission inventory used as forcing file for the flux calculation in the model. NH<sub>3</sub> emissions from the CEDS inventory describe two peaks: an important one in May and another smaller in September which are clearly observable in the CEDS depositions. CAMEO NH<sub>x</sub> depositions describe a pattern that differs from one region to another but with a peak in summer for most regions. The summer peak is also reflected in the emission seasonality as analyzed in Beaudor et al. (2023a). Both dry and wet NH<sub>x</sub> depositions from LMDZ-INCA have the same seasonal cycle except in East Africa, India and Latin America wherein these regions, wet depositions are largely dominants. Except in these regions, wet and dry depositions have similar contributions to the total depositions. In their study, Ge et al. (2022) found a higher contribution of dry deposition in almost all the continental regions. In the CCMi depositions, except for South-East Asia, variations over 320 the year are weak, with no clear seasonal pattern.

325

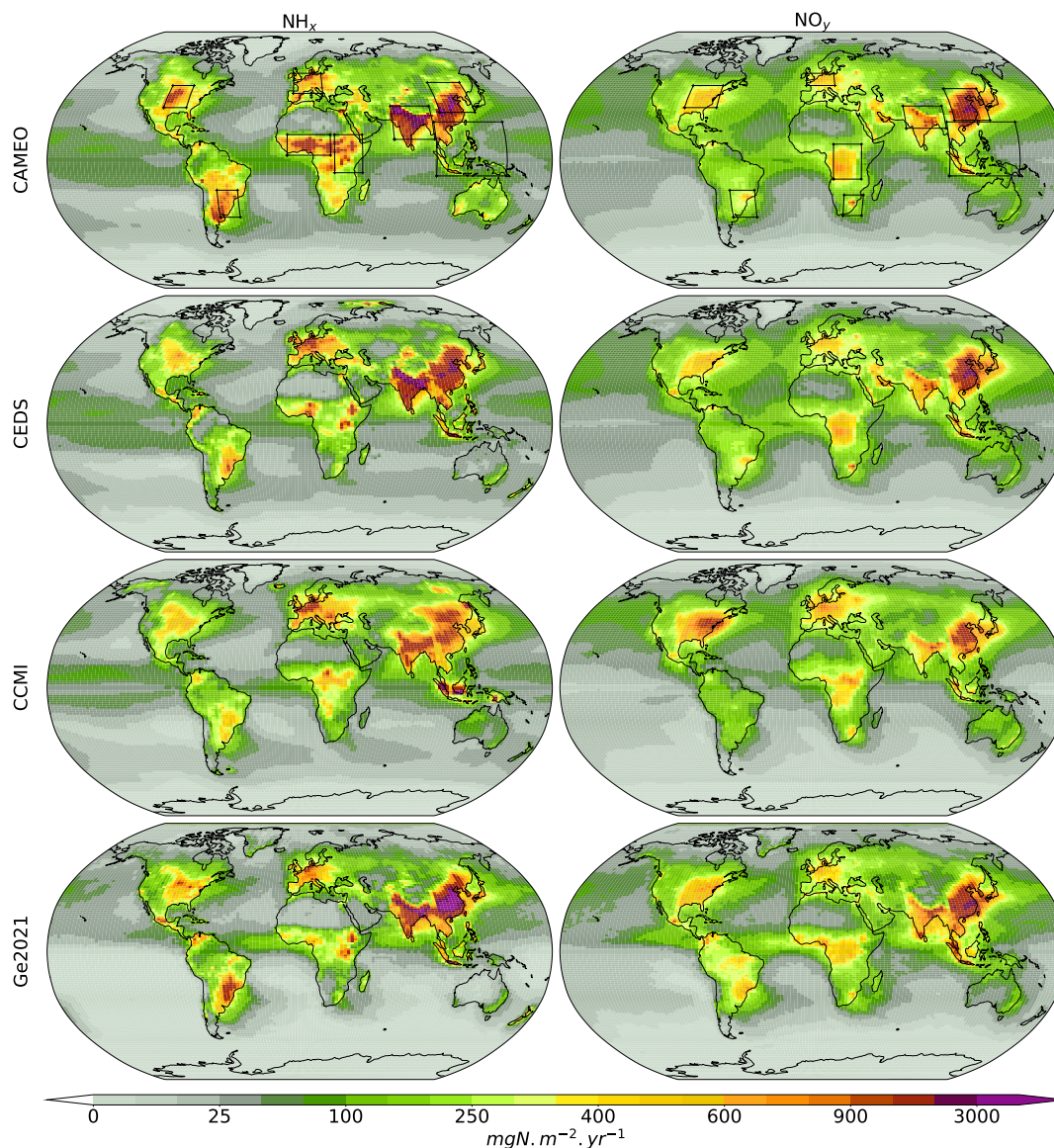


**Figure 8.** Annual mean total (dry + wet)  $\text{NH}_x$  (first column) and  $\text{NO}_y$  (second column) deposition for present-day conditions. The first row shows the N deposition fluxes calculated from the most recent CMIP exercise (IGAC/SPARC Chemistry–Climate Model Initiative (CCMI; Eyring et al., 2013, 2010–2014 climatology), second and third rows correspond to LMDZ-INCA simulations where CEDS and CAMEO emissions are prescribed respectively (2010–2014 climatology), last row display recent modelling results from Ge et al. (2022) using the EMEP model (2015). The black boxes in (a) and (b) delimit the regional bounds for the seasonal variability analysis. ( $\text{mgNm}^{-2}\text{yr}^{-1}$ ).

It is worth pointing out that LMDZ-INCA model uses a low effective  $\text{NH}_3$  Henry's law constant ( $= 74$ ) for the calculation of the wet deposition fluxes compared to other CTMs ( $100 - 3 \times 10^6$ ). In addition, no pH adjustment is considered for the  $\text{NH}_3$



Henry's law constant, while it appears to be important in controlling wet  $\text{NH}_3$  deposition. Bian et al. (2017) investigated the impact of pH-dependent  $\text{NH}_3$  wet deposition on atmospheric  $\text{NH}_3$  and associated nitrogen species with the Global Modeling Initiative (GMI) and found that without pH correction,  $\text{NH}_3$  wet deposition decreases significantly (from 17.5 to 1.1  $\text{TgNyr}^{-1}$ ). Because  $\text{NH}_3$  deposition has an impact on its atmospheric lifetime and, therefore, is an important factor in the ammonium-nitrate system, it would be interesting also to evaluate the sensitivity of the effective  $\text{NH}_3$  Henry's law constant and the consideration of the pH correction in LMDZ-INCA.

### 4.3.2 Nitrogen Oxide Deposition

$\text{NO}_y$  deposition patterns over Africa, India and China are consistent between the four estimates, especially for CEDS and CAMEO simulations and EMEP MSC-W (Figure 8). There are no major differences between CEDS and CAMEO simulated  $\text{NO}_y$  deposition fluxes since  $\text{NH}_3$  emissions have only a small impact on nitrate deposition. However, CCMI fluxes in the US and Europe (1300 and 900  $\text{mgN.m}^{-2}.\text{yr}^{-1}$ ) are more important than LMDZ-INCA (600 and 500  $\text{mgN.m}^{-2}.\text{yr}^{-1}$ ) and EMEP MSC-W (900 and 700  $\text{mgN.m}^{-2}.\text{yr}^{-1}$ ) depositions. On the opposite, in Latin America, CCMI depositions are the lowest. Global  $\text{NO}_y$  deposition budgets from CCMI and LMDZ-INCA vary between 39 and 43  $\text{TgN.yr}^{-1}$  while EMEP MSC-W estimate is 47  $\text{TgN.yr}^{-1}$  (Figure 7). Similarly as for  $\text{NH}_x$ , China, Africa and Latin America are the most important contributors to the global  $\text{NO}_y$  depositions budget in EMEP MSC-W and LMDZ-INCA estimates (about 47 %). CCMI estimates higher  $\text{NO}_y$  depositions in North America than in Latin America. The three regions Africa, North America and China account for half of the CCMI budget.

CCMI and LMDZ-INCA seasonal cycles of  $\text{NO}_y$  deposition are very well correlated together (see Figure S8 in the Supplementary Material). On the contrary of  $\text{NH}_x$  which are primarily driven by only a few sources of emissions (mainly agricultural  $\text{NH}_3$ ),  $\text{NO}_y$  are the results of  $\text{NO}_x$  sources and reactions involving several nitrate species. However,  $\text{NO}_x$  emissions mainly come from the energy, transportation, and industrial sectors (Hoesly et al., 2018; McDuffie et al., 2020) whose seasonal cycles are better-known than the agricultural one. Similarly as  $\text{NH}_x$ ,  $\text{NO}_y$  wet fluxes are contributing the most to the total depositions in most regions except in South Africa, Europe, and India where dry deposition dominates during several months. The main differences between CEDS and CAMEO are observed in the wet deposition in winter in Latin America and South Africa but also in India in summer and the whole year in southern-eastern Asia. It indicates that  $\text{NH}_3$  emissions rather impact wet  $\text{NO}_y$  deposition fluxes mostly when a direct loss through scavenging occurs such as during the monsoon season in India.

## 5 Impact of future emissions

### 5.1 Impact on atmospheric composition

Considering future CAMEO emissions under SSP5-8.5 and SSP4-3.4 in LMDZ-INCA highlights the range of possible impact of future  $\text{NH}_3$  emissions on N species and aerosol. Both scenarios of emissions lead to a global increase of the N species and aerosol burdens which also vary according to the  $\text{NO}_x$  and  $\text{SO}_2$  emission trends (Table 5).





**Table 5.** Tropospheric burden and deposition losses ( $\text{TgNyr}^{-1}$ ) of ammonia ( $\text{NH}_3$ ), ammonium particles ( $\text{NH}_4^+$ ), nitric acid ( $\text{HNO}_3$ ) and fine nitrate particles ( $\text{NO}_3^-$ ) for the present-day (2004-2014) and future (2090-2100) simulations.  $\text{N}_2\text{O}$  production through  $\text{NH}_3$  gas phase loss ( $\text{TgNyr}^{-1}$ ) is also included.

Simulation	Budget ( $\text{TgNyr}^{-1}$ )	$\text{NH}_3$	$\text{NH}_4^+$	$\text{HNO}_3$	$\text{NO}_3^-$
Present-day (2004-2014)					
CEDS	Burden	0.09	0.32	0.77	0.08
	Wet deposition	17.6	16.4	28.7	9.4
	Dry deposition	19.7	1.5	60.2	0.86
	Gas phase loss	0.74			
CAMEO	Burden	0.17	0.47	0.77	0.21
	Wet deposition	22.2	17.6	28.4	9.90
	Dry deposition	24.5	1.47	61.8	0.77
	Gas phase loss	1.00			
Future (2090-2100)					
CAMEO[585]	Burden	0.27	0.59	0.77	0.33
	Wet deposition	30.3	20.2	27.3	11.2
	Dry deposition	32.7	1.61	60.5	0.85
	Gas phase loss	1.28			
CAMEO[434]	Burden	0.36	0.65	0.77	0.38
	Wet deposition	35.6	21.3	26.8	11.7
	Dry deposition	39.0	1.73	59.7	0.90
	Gas phase loss	1.83			
CAMEO[434-126]	Burden	0.57	0.55	0.45	0.42
	Wet deposition	44.1	11.3	13.4	7.5
	Dry deposition	43.1	0.43	22	0.31
	Gas phase loss	1.58			
CAMEO[434-370]	Burden	0.35	0.71	0.72	0.45
	Wet deposition	38.7	21.6	24.6	13.2
	Dry deposition	42.3	1.87	61.1	1.15
	Gas phase loss	2.34			

360 Relatively to present-day level with CAMEO,  $\text{NH}_3$  burdens are increased by 37% in CAMEO[585], 50% in both CAMEO[434]  
 and CAMEO[434-370], and by 70% in CAMEO[434-126] which is considered as the 'higher' scenario regarding  $\text{NO}_x$  and  
 $\text{SO}_2$  emissions. In CAMEO[434-126], burden of  $\text{NH}_4^+$  ( $0.55 \text{ TgNyr}^{-1}$ ) is similar to the value of  $\text{NH}_3$  ( $0.57 \text{ TgNyr}^{-1}$ ) while  
 in both CAMEO[434] and CAMEO[434-370],  $\text{NH}_4^+$  burden ( $\sim 0.68 \text{ TgNyr}^{-1}$ ) is about twice the one of  $\text{NH}_3$ . Regarding the  
 nitrate burdens,  $\text{HNO}_3$  budget is similar to present-day value in CAMEO[434] and CAMEO[434-370] ( $\sim 0.17 \text{ TgNyr}^{-1}$ ), but  
 365 much smaller in CAMEO[434-126] (Table 5). It is explained by the lower  $\text{NO}_x$  emissions used in the later simulation com-  
 pared to the other simulations ( $9.1$  against  $38 \text{ TgNyr}^{-1}$ ) (see Table 1). However, the  $\text{NO}_3^-$  burden is within the same range of  
 values for the three future simulations ( $0.38$ - $0.45 \text{ TgNyr}^{-1}$ ) which is around twice as high as in the historical CAMEO run.





The impact of future CAMEO emissions under SSP4-3.4 on the distributions of  $\text{NH}_3$ ,  $\text{NO}_2$  and  $\text{HNO}_3$  surface concentrations are presented in Figure 9. Compared to the historical CAMEO simulation, CAMEO[SSPi] depicts large increases in  $[\text{NH}_3]$  of about  $5\text{--}10 \mu\text{g}\cdot\text{m}^{-3}$  over northern Africa, northern India and eastern China corresponding to the regions experiencing the most important increases in the agricultural  $\text{NH}_3$  emissions ( $> 4 \text{ gN}\cdot\text{m}^{-2}\cdot\text{yr}^{-1}$ , see Figure S1 in the Supplementary Material). As only negligible differences in the other future anthropogenic  $\text{NH}_3$  emissions are notable, the impact of the CAMEO[SSPi] on  $[\text{NH}_3]$  is similar for the three simulations. The impact on  $[\text{NO}_2]$  and  $[\text{HNO}_3]$  is much more contrasted between the simulations. In CAMEO[434], as the  $\text{NO}_x$  emissions are kept at their present-day level, no impact is observable. However, in CAMEO[434-126] and CAMEO[434-370] the  $\text{NO}_x$  emissions vary from the historical levels: in CAMEO[434-126], the emissions are much lower all over the globe while in CAMEO[434-370], emissions are largely reduced in the most developed countries (Europe, China, and the US) and increased in the Southern Hemisphere along with India and the Gulf States. It leads to a decrease of around  $5$  to  $12 \mu\text{g}\cdot\text{m}^{-3}$  in  $[\text{NO}_2]$  and of  $1$  to  $3 \mu\text{g}\cdot\text{m}^{-3}$  in  $[\text{HNO}_3]$  over China, Europe and the US in CAMEO[434-126]. In CAMEO[434-370], the impact of the future emissions on both  $[\text{NO}_2]$  and  $[\text{HNO}_3]$  also follows  $\text{NO}_x$  emission trends with most important increases located in India ( $15$  and  $8 \mu\text{g}\cdot\text{m}^{-3}$ , respectively) and smaller decrease situated in Europe, China, and the US.

As a result of these changes in nitrate precursor surface concentrations, nitrate and sulfate particles are expected to vary significantly in the future. In order to understand future patterns in the nitrate and sulfate aerosol formations, the state of ammonia neutralization of the sulfuric and nitric acids is shown for different pressure levels in Figure 11.

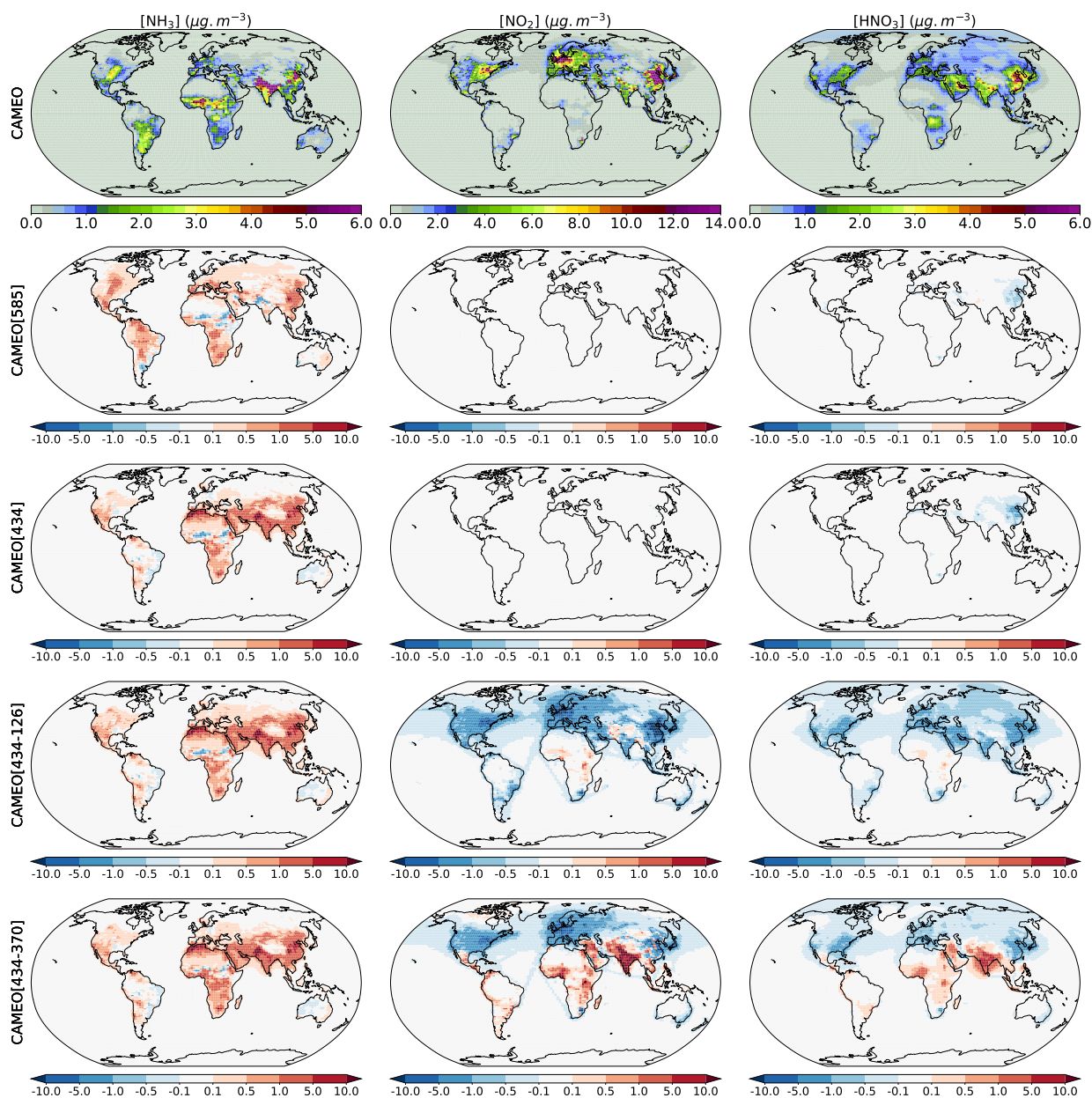


**Figure 9.** Mean annual surface concentrations of  $\text{NH}_3$ ,  $\text{NO}_2$  and  $\text{HNO}_3$  simulated in the CAMEO simulation (1st row; over 2004-2014) and the anomalies between the CAMEO[SSPi] and CAMEO simulations ([SSPi]:585, 434, 434-126 and 434-370 in rows 2-5; over 2090-2100) ( $\mu\text{g}\cdot\text{m}^{-3}$ ).



Four chemical domains can be derived from the simulated relative abundances of  $\text{NH}_3$ ,  $\text{NH}_4^+$ ,  $\text{NO}_3^-$ ,  $\text{HNO}_3$  and  $\text{SO}_4^{2-}$   
385 (Metzger et al., 2002; Xu and Penner, 2012; Hauglustaine et al., 2014; Paulot et al., 2016; Ge et al., 2022) First, we define the  
total molar concentrations of sulfate ( $T_S$ ), nitrate ( $T_N$ ), ammonia ( $T_A$ ) and ammonia needed to fully neutralize the sulfate  
( $T_{A\text{-free}}$ ):

$$T_S = [\text{SO}_4^{2-}], \quad (1)$$

390  $T_N = [\text{NO}_3^-] + [\text{HNO}_3], \quad (2)$

$$T_A = [\text{NH}_3] + [\text{NH}_4^+], \quad (3)$$

$$T_{A\text{-free}} = T_A - 2 \times T_S \quad (4)$$

395 The four chemical domains are defined as : sulfate very rich ( $T_A / T_S < 1$ ), sulfate rich ( $1 < T_A / T_S < 2$ ), nitrate rich ( $0$   
<  $T_{A\text{-free}}/T_N < 1$ ) and ammonia rich ( $T_{A\text{-free}}/T_N > 1$ ). When  $T_{A\text{-free}} / T_N > 1$ , sufficient ammonia remains to react with  
nitrate to form  $\text{NH}_4\text{NO}_3$ . The resulting calculated domains are illustrated in Figure 11. In order to focus on the most important  
anthropogenic sources, we imposed a threshold on the secondary inorganic aerosol (SIA) concentration which is set as  $(\text{NH}_4^+$   
+  $\text{NO}_3^- + \text{SO}_4^{2-}) \geq 0.5 \mu\text{g.m}^{-3}$ . This threshold has been arbitrarily chosen similarly as in Ge et al. (2022). In rich and very  
400 rich  $\text{SO}_4^{2-}$  domains (yellow and blue areas in Figure 11), not all of the sulfuric acid is neutralized ( $\text{SO}_4^{2-}$  not only exists as in  
 $\text{NH}_4\text{SO}_4$ ). This is the case, for instance, at the surface in the regions where high  $\text{SO}_2$  sources are collocated with low  $\text{NH}_3$   
sources. In the CAMEO simulation, these areas are rather located in the Sahara, northern Russia, and along the coastlines in  
Asia, the western US, and the Arabian sea. These regions expand over the continents as we move away from the surface (at  
900 hPa). It is explained by the reduced amount of  $\text{NH}_3$ , which is easily converted into  $\text{NH}_4^+$  at lower pressure levels (900  
405 hPa and 500 hPa). In green and red areas all of the sulfuric acid has been neutralized and excess of  $\text{NH}_3$  is available to react  
with  $\text{HNO}_3$  to form  $\text{NH}_4\text{NO}_3$ . Most continental regions characterized by important anthropogenic activities are under these  
regimes at the surface. Considered nitrate-rich, these regions are rather continental and remote from the main  $\text{NH}_3$  hotspot as in  
the Middle East for example. They are generally characterized by high  $\text{NO}_x$  emissions or large transport of  $\text{NO}_x$  and relatively  
rapid deposition of  $\text{NH}_x$ . Finally, red areas correspond to regions where ammonia prevails and the availability of nitrate limits  
410 the formation of  $\text{NH}_4\text{NO}_3$ . It is the most dominant regime on the surface, covering most of the continents and especially the  
places with the most intensive agricultural activities (Asia, Europe, southern and northeastern Africa, and the US).

By analyzing the change in the state of ammonia neutralization of sulfuric and nitric acids between the different simulations  
through Figure 11, we investigate the impact of the future emissions on the different surface aerosol concentrations shown in  
Figure 10.

415 Only small positive changes in China in the  $[\text{NO}_3^-]$  ( $< 2 \mu\text{g.m}^{-3}$ ) are observable in CAMEO[434] and CAMEO[585]  
compared to the CAMEO simulation. Particularly in this region, a shift from nitrate-rich to ammonia-rich is notable at 900 hPa

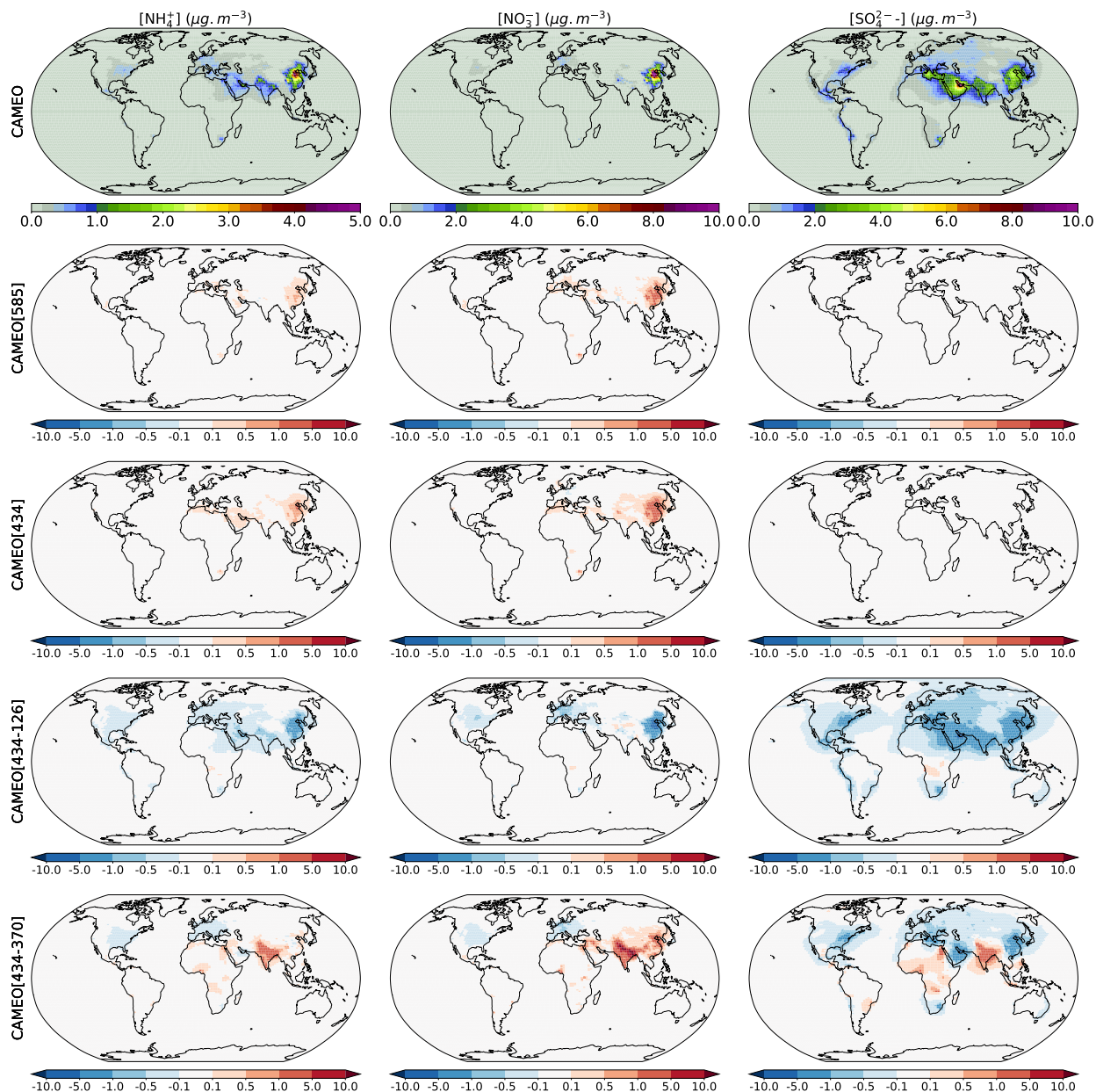


**Figure 10.** Mean annual surface concentrations of  $\text{NH}_4^+$ ,  $\text{NO}_3^-$  and  $\text{SO}_4^{2-}$  simulated in the CAMEO simulation (1st row; over 2004-2014) and the anomalies between the CAMEO[SSPi] and CAMEO simulations ([SSPi]:585, 434, 434-126 and 434-370 in rows 2-5; over 2090-2100) ( $\mu\text{g.m}^{-3}$ ).

which is explained by relatively higher  $[\text{NH}_3]$  and a stronger limitation by  $\text{HNO}_3$  availability. It is a result of much higher  $\text{NH}_3$  emissions and no change in other emissions in this scenario. In another hand, CAMEO[434-126] depicts important negative



anomalies of  $[\text{NH}_4^+]$ ,  $[\text{NO}_3^-]$  and  $[\text{SO}_4^{2-}]$  especially in China ( $> 4 \mu\text{g}\cdot\text{m}^{-3}$ ). In China, the ammonia-rich conditions observed  
420 in CAMEO are expanded (less fine PM are formed) as we reach 900 hPa, highlighting the abundance of gaseous ammonia.  
In CAMEO[434-126], even though more  $\text{NH}_3$  is emitted, important reductions in  $\text{NO}_x$  and  $\text{SO}_2$  emissions are notable (see  
Figure S1 in the Supplementary Material). It means that almost no acids are available to react with ammonia and therefore it  
is not converted into ammonium and its gaseous-form concentration is enhanced. A similar situation arose attention in China  
in the last decades, where an unexpected increase in the  $[\text{NH}_3]$  has been observed after strong regulations in  $\text{NO}_x$  and  $\text{SO}_2$   
425 emissions and no change in the  $\text{NH}_3$  emissions (Lachatre et al., 2019). Compared to this later study, the effect in CAMEO[434-  
126] is even stronger on  $[\text{NH}_3]$  due to an increase in the  $\text{NH}_3$  emissions. This is also confirmed by comparing  $[\text{NH}_3]$  from  
CAMEO[434-126] and CAMEO[434] where  $\text{NH}_3$  emissions are identical but a slightly stronger impact on the concentrations  
is highlighted for instance in India, in Europe and the US (Figure 9).  $[\text{SO}_4^{2-}]$  in CAMEO[434-126] also decreases considerably  
over the Arabian Peninsula, India, and the western US (of about  $2\text{-}4 \mu\text{g}\cdot\text{m}^{-3}$ ) which is a direct consequence of the  $\text{SO}_2$   
430 regulations in scenario SSP1-2.6. The shift in the emissions in CAMEO[434-370] compared to CAMEO for the present-day  
highlights positive anomalies in the N inorganic aerosols concentrations over northern India (around  $+ 3 \mu\text{g}\cdot\text{m}^{-3}$  in  $[\text{NH}_4^+]$   
and  $+ 5 \mu\text{g}\cdot\text{m}^{-3}$  in  $[\text{NO}_3^-]$ ). The enhanced aerosol formation in this region is due to the important increase in  $\text{NH}_3$  emissions  
along with the highest  $\text{NO}_x$  and  $\text{SO}_2$  emissions. The formation of the secondary inorganic aerosol is very sensitive to the  $\text{NO}_x$   
and  $\text{SO}_2$  emissions, as demonstrated by the distinct responses between CAMEO[434], CAMEO[434-126], CAMEO[434-370]  
435 while  $\text{NH}_3$  levels are similar in the three simulations (Figure 10). Interesting patterns also arise in CAMEO[434-370] in  
regions situated in Africa which are characterized by a very rich  $\text{NH}_3$  domain not observable in the other simulations (Figure  
11). Contrary to India where both  $\text{NO}_3^-$  and  $\text{SO}_4^{2-}$  formations are favored, significant increases in  $[\text{SO}_4^{2-}]$  only are observed  
in Africa. It is likely that in Africa,  $\text{HNO}_3$  availability is still limited to react with the excess of ammonia despite the small  
increases in  $\text{NO}_x$  emissions under SSP3-7.0. Over Europe and the US, a notable decrease of  $[\text{SO}_4^{2-}]$  (around  $- 1 \mu\text{g}\cdot\text{m}^{-3}$ )  
440 is observed. It is a direct consequence of lower levels of  $\text{NO}_x$  and  $\text{SO}_2$  along with constant levels of  $\text{NH}_3$  leading to less  
ammonium-related aerosol formation as shown in Figure 10. Finally, the evolution of the neutralization state by ammonia is  
also notable throughout the vertical profile and is particularly distinctly influenced by  $\text{NO}_x$  and  $\text{SO}_2$  levels. In CAMEO[434-  
370], the ammonia-rich state remains predominant not only at the surface but also at 900 hPa likely enhanced by convection that  
transports the excess of ground ammonia to more elevated layers. Additionally, at this altitude, we note the emergence of coastal  
445 nitrate-rich regions in West Africa, India and East Asia. By moving further from the surface to the upper troposphere, nitrate-  
rich regions expand across Africa, the Middle East and Asia indicating non negligible impacts on tropospheric chemistry.

## 5.2 Impact on nitrogen surface deposition

Finally, the impact of the future emissions on the  $\text{NH}_x$  and  $\text{NO}_y$  surface deposition is depicted in Figure 12. Independently  
of the  $\text{NO}_x$  and  $\text{SO}_2$  scenario,  $\text{NH}_x$  deposition increases significantly. Total  $\text{NH}_x$  deposition is estimated to increase from 65  
450  $\text{TgNyr}^{-1}$  to 98-105  $\text{TgNyr}^{-1}$  with the lowest and highest value reached in respectively, CAMEO[434] and CAMEO[434-  
370] (Table 5). Regionally, increases in  $\text{NH}_x$  deposition can reach  $2000 \text{mgN}\cdot\text{m}^{-2}\cdot\text{yr}^{-1}$  (Figure 12) and are mostly located in  
areas where  $\text{NH}_3$  emissions are enhanced under SSP4-3.4 (northern Africa, India and China). This large increase is mostly due



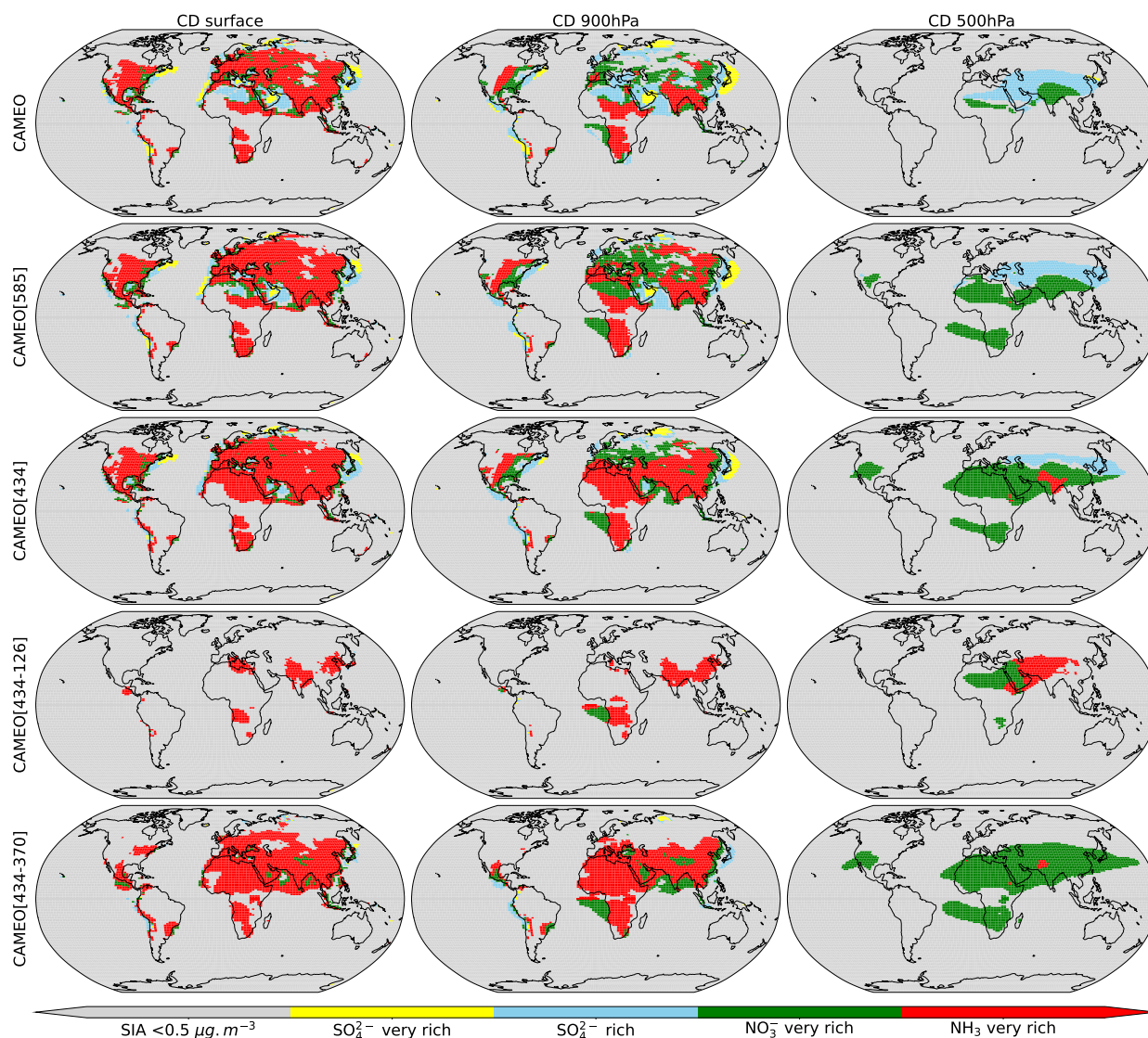


**Figure 11.** The state of ammonia neutralization of sulfuric and nitric acids for areas where secondary inorganic aerosol concentration in the fine particle fraction (PM<sub>2.5</sub>) is  $> 0.5 \mu\text{g.m}^{-3}$  calculated from the different simulations (averages done over 2004-2014 for CAMEO and over 2090-2100 for CAMEO[SSPi]) at the surface, 900 hPa and 500 hPa (first, second and third columns). The four chemical domains are defined as : sulfate very rich ( $T_A / T_S < 1$ , yellow area), sulfate rich ( $1 < T_A / T_S < 2$ , blue areas), nitrate rich ( $0 < T_{A-free} / T_N < 1$ , green areas) and ammonia rich ( $T_{A-free} / T_N > 1$ , red areas).

to enhanced total  $\text{NH}_3$  deposition while  $\text{NH}_4^+$  deposition either increases slightly (around  $+ 4 \text{ TgNyr}^{-1}$ ) or even decreases, for example, in CAMEO[434-126] ( $-7 \text{ TgNyr}^{-1}$ ). In this latter case,  $\text{NH}_4^+$  deposition decreases as a result of a shift in the  
 455 chemical regime where most of  $\text{NH}_3$  does not neutralize sulfuric and nitric acids and remains in its gaseous phase due to





lower  $[\text{NO}_x]$  and  $[\text{SO}_2]$ . Therefore, in parallel to less  $\text{NH}_4^+$  deposition in CAMEO[434-126], more  $\text{NH}_3$  deposition occurs. Regarding the future  $\text{NO}_y$  deposition, the results are more contrasted between the different simulations. In both CAMEO[434] and CAMEO[434-370] simulations, total  $\text{NO}_y$  deposition keeps a constant value close to the present-day simulation ( $\sim 100 \text{ TgNyr}^{-1}$ ) because of a similar decrease in  $\text{HNO}_3$  deposition and increase in  $\text{NO}_3^-$  deposition ( $2\text{-}4 \text{ TgNyr}^{-1}$ ). Compared to  
460 CAMEO, the total  $\text{NO}_y$  deposition is reduced by more than half in CAMEO[434-126] ( $\sim 58 \text{ TgNyr}^{-1}$ ) as a result of a decrease in both  $\text{NO}_3^-$  and  $\text{HNO}_3$  depositions.

As expected, no changes in the  $\text{NO}_y$  deposition occur spatially between CAMEO and CAMEO[434] due to identical  $\text{NO}_x$  emissions (Figure 12). Under the low  $\text{NO}_x$  scenario (CAMEO[434-126]),  $\text{NO}_y$  deposition decreases all over the globe, and the highest anomalies are located in China ( $< -800 \text{ mgN.m}^{-2}.\text{yr}^{-1}$ ). When future SSP3-7.0 emissions of  $\text{NO}_x$  are pre-  
465 scribed, the impact on  $\text{NO}_y$  deposition follows a similar pattern as  $\text{NO}_x$  emissions. Compared to CAMEO,  $\text{NO}_y$  deposition in CAMEO[434-370] is significantly increased in India ( $> 800 \text{ mgN.m}^{-2}.\text{yr}^{-1}$ ) and at a lower extent in Africa and the Arabian Peninsula ( $\sim 300 \text{ mgN.m}^{-2}.\text{yr}^{-1}$ ). Over the most developed countries,  $\text{NO}_y$  deposition depicts negative anomalies of around  $300 \text{ mgN.m}^{-2}.\text{yr}^{-1}$ .

### 5.3 Associated radiative forcing

470 The impact of the different future emissions on the total nitrate, and sulfate AOD at 550 nm is presented in Figure 13 and Table 6. The global increase in the nitrate AOD due to future  $\text{NH}_3$  emissions from CAMEO ranges from 50% to 100% for CAMEO[434-370]. As seen in the previous section, considering future SSP4-3.4  $\text{NH}_3$  emissions from CAMEO and keeping the other emissions at their present-day level (CAMEO[434]) has a positive impact on the nitrate aerosol formation which leads to an increase comprised between 0.01 for most lands and oceans to 0.05 over China of the total AOD. While sulfate  
475 AOD contributed the most to the total AOD with present-day level emissions, nitrate AOD becomes very much important in CAMEO[434]. When considering strict regulations in the  $\text{NO}_x$  and  $\text{SO}_2$  emissions as in CAMEO[434-126], the impact on the AOD is significant for the sulfate aerosol depth where the decrease can reach  $-0.15$  over China, for instance, compared to the CAMEO simulation. The positive impact on the nitrate AOD in this simulation is of the same range as the one in CAMEO[434] except in China where the decrease in  $\text{NO}_x$  emissions leads to a decrease in the AOD of around 0.03. Except  
480 in tropical Africa where there is almost no impact of future emissions on the sulfate AOD, most of the land regions depict negative anomalies in the total AOD. Finally, the impact of future  $\text{NO}_x$  and  $\text{SO}_2$  emissions from SSP3-7.0 combined with  $\text{NH}_3$  emissions from SSP4-3.4 leads to a strong increase in the total AOD over Africa and India (of around 0.10 and 0.15, respectively) and a slight decrease over western US and Europe (around 0.03). The highest increases in the total AOD are explained by large positive anomalies in the nitrate and sulfate AOD (the impact on nitrate is around three times higher than on  
485 sulfate) while the negative patterns are mostly the result of negative anomalies in the sulfate AOD and slight changes in nitrate AOD. The different impacts on the total AOD inform about the importance of not only considering ammonia behavior alone but accounting for  $\text{NO}_x$  and  $\text{SO}_2$ , especially in the context of emission mitigation policies. It is important to note that global present-day nitrate AOD in CAMEO is twice higher (0.016; Table 6) than the average quantified in the intercomparison from AeroCom Phase III but close to the GISS model estimate (0.015). However, global sulfate AOD in CAMEO (0.042) is in the

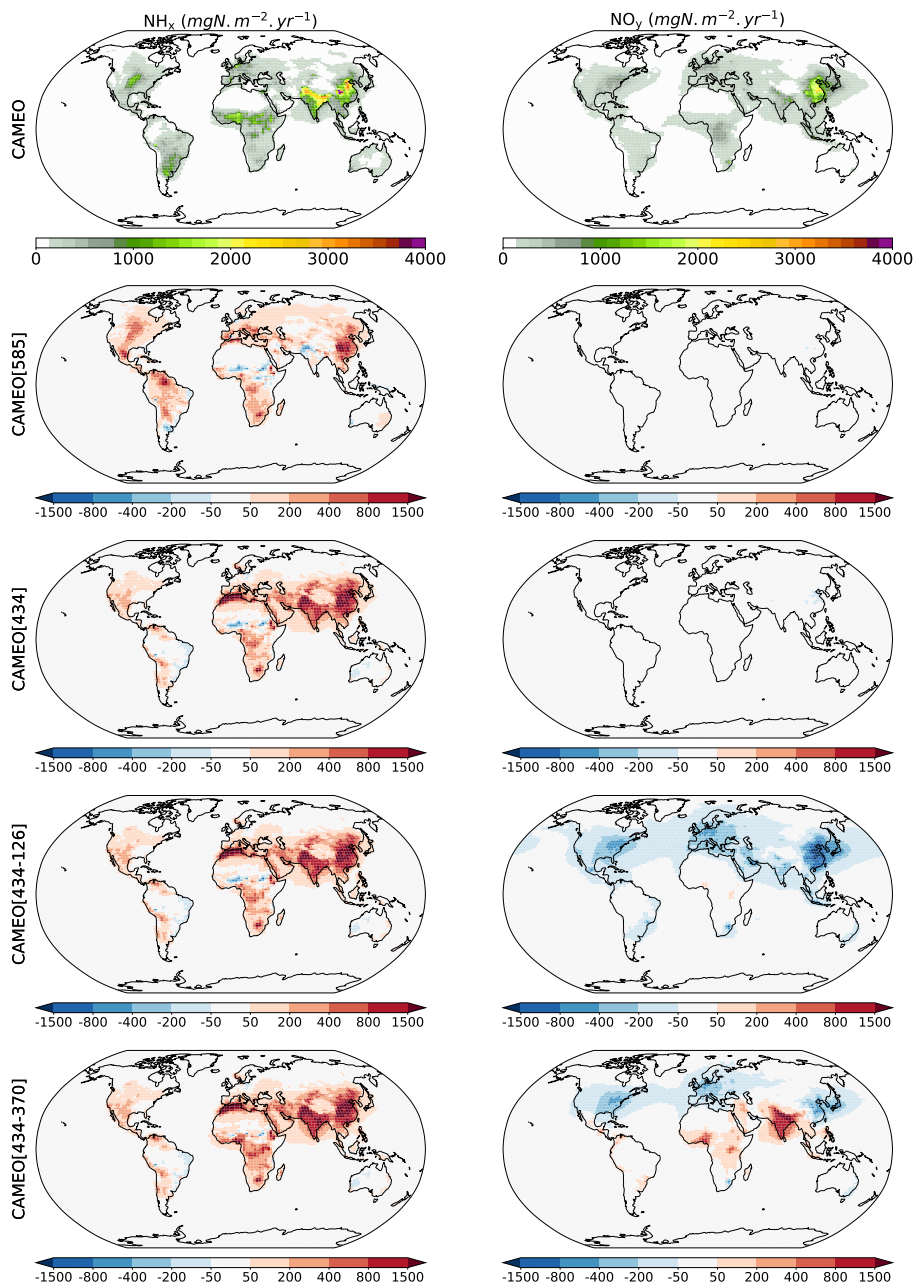


**Figure 12.** Mean annual surface depositions of  $\text{NH}_x$  and  $\text{NO}_y$  simulated in the CAMEO simulation (1st row; over 2004-2014) and the anomalies between the CAMEO[SSPi] and CAMEO simulations ([SSPi]:585, 434, 434-126 and 434-370 in rows 2-5; over 2090-2100) ( $\text{mgN.m}^{-2}.\text{yr}^{-1}$ ).



490 recent model range (0.047) presented by Bian et al. (2017). The all-sky direct radiative forcings at the top of the atmosphere (RF TOA) are presented in Table 6 and are calculated as the difference between the CAMEO[SSPi] and CAMEO experiments. Only replacing historical NH<sub>3</sub> emissions with those from SSP585 and SSP434 results in a net cooling of -114 mW.m<sup>-2</sup> and -160 mW.m<sup>-2</sup> induced by nitrate aerosol radiative forcing and a slight positive warming from the sulfate forcing (≈ 3 mW.m<sup>-2</sup>). The nitrate aerosol effects of the other experiments (CAMEO[434-126] and CAMEO[434-370]) are much more  
 495 important (-164 and -243 mW.m<sup>-2</sup>) than the highest anthropogenic radiative forcing calculated by Hauglustaine et al. (2014) which compares the scenario RCP8.5 for 2100 with pre-industrial conditions (-115 mW.m<sup>-2</sup>). The sulfate aerosol radiative effect is 7 times more important in CAMEO[434-126] (343 mW.m<sup>-2</sup>) than in CAMEO[434-370] where both NO<sub>x</sub> and SO<sub>2</sub> emissions from SSP126 are highly slow down in 2100.

**Table 6.** All-sky direct radiative forcing at the top of the atmosphere (RF TOA; mW.m<sup>-2</sup>) and aerosol optical depth (AOD) of the nitrate and sulfate aerosols since the present-day and future evolution under the different scenarios considered in this study. Note that for AOD, future evolution is given as ΔAOD as the difference between the future and present-day AODs.

		NO <sub>3</sub> <sup>-</sup>	SO <sub>4</sub> <sup>2-</sup>
Present-day (2004-2014)			
CAMEO	AOD	0.016	0.042
Future (2090-2100)			
CAMEO[585]	ΔAOD	0.008	-0.0002
	RF (TOA)	-114	1.9
CAMEO[434]	ΔAOD	0.011	-0.0002
	RF (TOA)	-160	4
CAMEO[434-126]	ΔAOD	0.012	-0.026
	RF (TOA)	-164	343
CAMEO[434-370]	ΔAOD	0.016	-0.003
	RF (TOA)	-243	46

#### 5.4 Impact on N<sub>2</sub>O production

500 The oxidation of ammonia with the hydroxyl (OH) radical into N<sub>2</sub>O is an additional atmospheric pathway that can represent an important climate factor in the future. Multiple studies investigated the importance of the production of N<sub>2</sub>O from NH<sub>3</sub> which can range from 0.6 to 1.8 Tg(N<sub>2</sub>O)<sub>yr</sub><sup>-1</sup> (Dentener and Crutzen, 1994; Kohlmann and Poppe, 1999; Hauglustaine et al., 2014; Pai et al., 2021). Our present-day production matches well with this range (1.6 Tg(N<sub>2</sub>O)<sub>yr</sub><sup>-1</sup>, Table 5) and represent 15 % of the present-day total anthropogenic N<sub>2</sub>O emissions used for CMIP6 (Gidden et al., 2018). However, considering  
 505 that natural soil emission contribution (10 Tg(N<sub>2</sub>O)<sub>yr</sub><sup>-1</sup>) is as important as the total anthropogenic source as estimated by Tian et al. (2024), our present-day production would in fact, represent 8% of the total N<sub>2</sub>O emissions. When considering our highest future NO<sub>x</sub> scenario (SSP3-7.0) combined with NH<sub>3</sub> emissions from SSP4-3.4, N<sub>2</sub>O production accounts for 18%

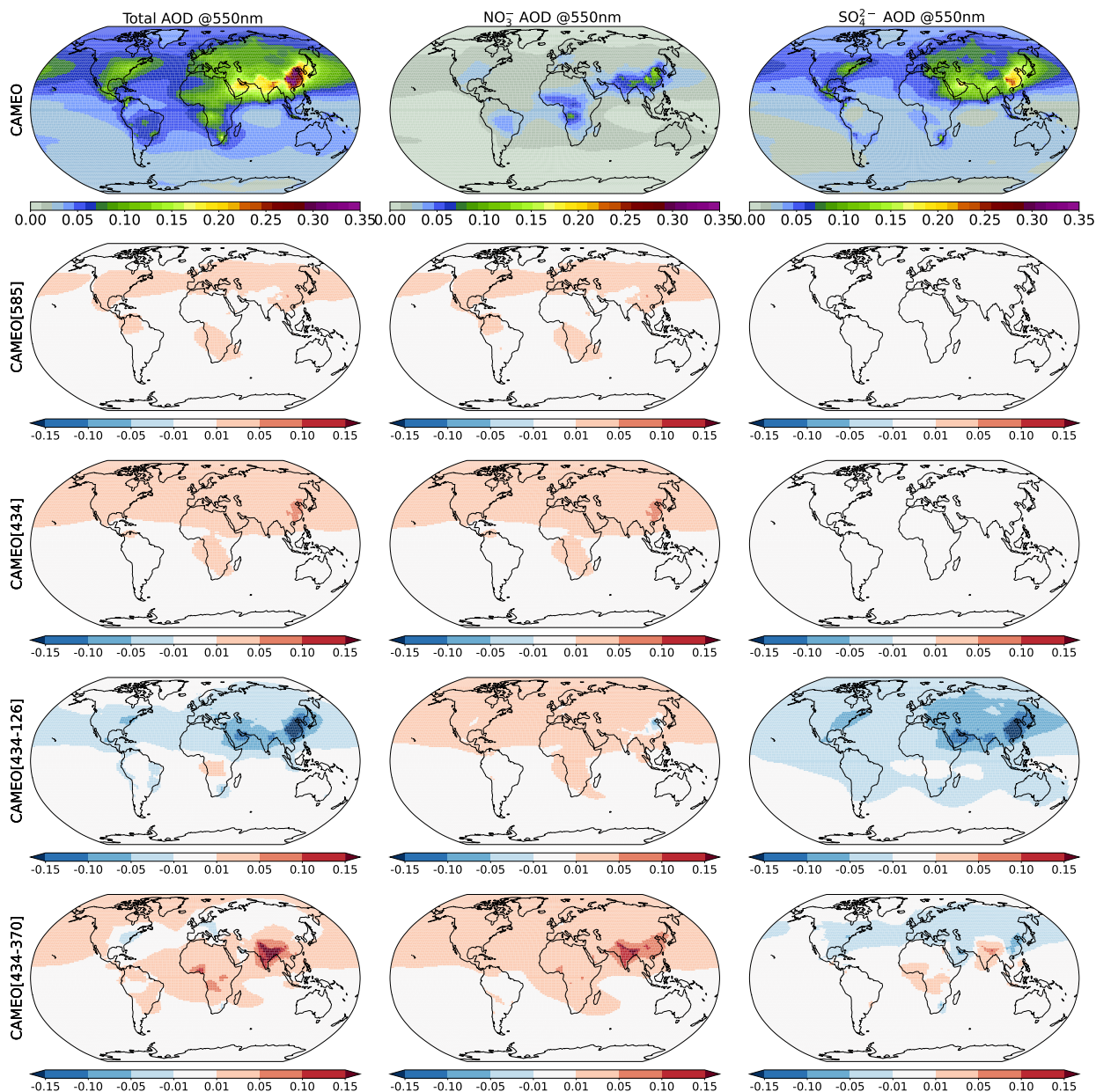


**Figure 13.** Mean annual total anthropogenic aerosol (i.e.: nitrate + sulfate AOD; first column), nitrate aerosol (second column), and sulfate aerosol (third column) optical depths at 550nm simulated in the CAMEO simulation (1st row; over 2004-2014) and the anomalies between the CAMEO[SSPi] and CAMEO simulations ([SSPi]:585, 434, 434-126 and 434-370 in rows 2-5; over 2090-2100).

(2.9 Tg(N<sub>2</sub>O)yr<sup>-1</sup>) of the future N<sub>2</sub>O anthropogenic emissions (under SSP3.70, Gidden et al., 2018). This result is close to the 21% quantified by Pai et al. (2021) using RCP trajectories for 2100.



## 510 6 Summary and conclusions

Because  $\text{NH}_3$  impacts on the nitrate aerosol and nitrous oxide levels in the atmosphere, change in agricultural  $\text{NH}_3$  emissions have important implications for climate and air quality. Regulating agricultural practices is a challenge due to its importance in feeding the population and thus, understanding the impact of future agricultural  $\text{NH}_3$  emissions on the atmospheric chemistry, is of high interest to design accurate mitigation emission scenarios. In this paper, the LMDZ-INCA global model is exploited to evaluate the impact of a new agricultural  $\text{NH}_3$  emission dataset recently developed based on the ORCHIDEE Land Surface Model. This new dataset investigates the role played by  $\text{NH}_3$  emissions in the atmosphere considering the dynamical environmental conditions and accounting for natural soil sources. The model results have been compared to  $\text{NH}_3$  columns observed by the IASI instrument but also to surface concentrations measured by various observational networks. In addition, in LMDZ-INCA, tropospheric aerosols are also included through a representation of the sulfate nitrate–ammonium cycle and heterogeneous reactions between gas-phase chemistry and aerosols. With this model, we investigate the impact of present-day and future (2090-2100)  $\text{NH}_3$  emissions on atmospheric composition, N deposition fluxes and climate forcing.

The key results of this paper are summarized as follows :

1.  $\text{NH}_3$  emissions provided by CAMEO show good accuracy in the simulated  $\text{NH}_3$  columns when evaluated against the IASI observations. Large reductions in the spatial model biases are noticeable compared to the reference version where the CEDS inventory is prescribed. More specifically, the biases decreased by at least 50 % in Africa, Latin America, and the US. CAMEO emissions not only improved the spatial representation of the columns, but also their seasonal cycle, especially in India, Equatorial Africa, China, and South America, where the skill functions calculated for the temporal variability gained between 1 to 3 points compared to the CEDS simulation. Comparisons of the simulated surface observations with ground-based observations indicate that using CAMEO emissions improved the representation of both annual  $\text{NH}_3$  and  $\text{NO}_3^-$  concentrations at the surface in 2015 in China, the US, and Canada. In Europe, the reduction of the  $\text{NH}_3$  bias however does not lead to improvement in the aerosol representation compared to CEDS.
2. The impact of CAMEO  $\text{NH}_3$  emissions on  $\text{NH}_x$  and  $\text{NO}_y$  deposition fluxes has been investigated. The global budget of  $\text{NH}_x$  is around  $65 \text{ TgNyr}^{-1}$  which is 20 % higher than the average calculated from other model-based estimates (CCMI, EMEP MSC-W and CEDS). The difference is mainly explained by enhanced deposition in Africa which is twice the budget from the three estimates. Due to relatively low nitrate levels and much higher emissions in equatorial Africa, more  $\text{NH}_3$  is removed through deposition processes, especially during the precipitation season when wet scavenging occurs more frequently. Despite differences with the EMEP and CCMI modelling results, a seasonal comparison at a specific measurement station from the INDAAF network in western Africa shows good correlations in the  $\text{NH}_4^+$  wet deposition when CAMEO emissions are used in the LMDZ-INCA model.
3. Our analysis of the  $\text{NH}_x$  deposition seasonal cycle highlights some discrepancies in the simulated fluxes from CCMI where seasonal variation is deficient. The CCMI dataset is a crucial forcing file for ESM more specifically for Land Surface Models. Even though the agricultural sector is the major driver for  $\text{NH}_3$  emission seasonality,  $\text{NH}_x$  deposition





545 can also play a role in more remote regions characterized by intensive precipitation seasons. Bi-directional flux of  
NH<sub>3</sub> can significantly impact NH<sub>3</sub> deposition, emission, reemission, and atmospheric lifetime Sutton et al. (2007). The  
interactive calculation of the different fluxes between the surface and the atmosphere has already been implemented  
in modeling approaches and shows significant improvements in the [NH<sub>3</sub>], [NH<sub>4</sub><sup>+</sup>], [NO<sub>3</sub><sup>-</sup>] and NH<sub>4</sub><sup>+</sup> wet depositions  
at regional and global scale (Pleim et al., 2019; Vira et al., 2019, 2022). This aspect motivates the implementation of  
a coupling based on a compensation point for NH<sub>3</sub> between LMDZ-INCA and ORCHIDEE, which is already under  
development. The coupling seems promising to improve, for instance, the overestimation from CAMEO emissions and  
550 the resulting NH<sub>3</sub> columns over the US and Europe in July.

4. Even though we are aware of some uncertainties and potential room for improvement, the model evaluation provides  
some confidence for using CAMEO emissions to investigate the impact of future NH<sub>3</sub> emissions on atmospheric chem-  
istry and climate. We have constructed four future scenarios for 2090-2100 in which the impact of CAMEO emissions  
for SSP5-8.5 and SSP4-3.4 under different NO<sub>x</sub> and SO<sub>2</sub> emission conditions has been studied. It is worth noticing that  
555 as far as we know, no future gridded livestock and interactive soil emissions have been used to investigate future NH<sub>3</sub>  
emission perturbations on the atmospheric chemistry at the global scale.

5. Future CAMEO emissions lead to an overall increase of the global NH<sub>3</sub> burden ranging from 37% to 70% while NO<sub>3</sub><sup>-</sup>  
burden increases by 38% - 50% depending on the scenario. By analyzing the behavior of CAMEO[434], we investigated  
the isolated impact of future NH<sub>3</sub> emissions. Our results highlight small changes in the nitrate formation mainly over  
560 eastern Asia, more specifically China (+ 2 μg.m<sup>-3</sup>) where nitrate concentrations are high (HNO<sub>3</sub> > 6 μg.m<sup>-3</sup>) and thus  
ammonium neutralization is possible. It leads to an increase of around 0.05 in the total nitrate and sulfate AOD in China  
and a global increase of 19%. In CAMEO[434-126], in which NO<sub>x</sub> and SO<sub>2</sub> emissions are highly decreasing compared to  
present-day, we observed important decreases in surface nitrate and sulfate aerosol concentrations, especially over China  
(-4 μg.m<sup>-3</sup>). In this scenario, even though NH<sub>3</sub> emissions increase the global nitrate AOD (+0.016), the negative impact  
565 of sulfate aerosol AOD is more important (-0.026), which results in a total AOD reduction of 23%. In CAMEO[434-  
126], the increase in the total nitrate burden and AOD indicates that despite less nitrate being formed at the surface, more  
nitrate is vertically uplifted in the upper troposphere. When combined with increased NO<sub>x</sub> and SO<sub>2</sub> emissions, higher  
NH<sub>3</sub> emissions lead to an enhanced formation of aerosol (+5 μg.m<sup>-3</sup> of NO<sub>3</sub><sup>-</sup>) at the surface compared to present-day  
levels as is the case over India in CAMEO[434-370]. Despite the decrease of NO<sub>x</sub> and SO<sub>2</sub> emissions over China, the  
570 US, Europe, and Saudi Arabia, the total nitrate and ammonium burden is doubled due to the contribution of India as one  
of the highest hotspots in terms of aerosol ammonium nitrate precursors in this scenario. In addition, India and Africa  
are the regions experiencing the highest change in the total nitrate and sulfate AOD (+80 to +100 %) due to a higher  
contribution of the nitrate AOD.

6. In addition to the impact on the air quality and climate, future NH<sub>3</sub> emissions have a positive impact on the total  
575 NH<sub>x</sub> deposition fluxes over land and oceans (+35%). As already mentioned, the coupling between LMDZ-INCA and  
ORCHIDEE would improve the representation of the N exchanges. In the framework of new future simulations with





a consideration of climate change, emissions would also change under the increase of temperatures, for example. In addition to the direct impact of climate change on the emissions and deposition fluxes, one could also expect a change coming from the land-use shift due to its influence on the deposition velocity for instance.

- 580 7. Radiative forcings associated with the aerosol formation in the different scenarios have been presented. The impact of future CAMEO emissions alone results in a net cooling from nitrate aerosols which ranges from  $-114 \text{ mW}\cdot\text{m}^{-2}$  to  $-160 \text{ mW}\cdot\text{m}^{-2}$ . By varying the future sulfate and nitrate emissions, the nitrate radiative effect can either overshoot (net total impact of  $-200 \text{ mW}\cdot\text{m}^{-2}$ ) or be offset by the sulfate effect (net total impact of  $+180 \text{ mW}\cdot\text{m}^{-2}$ ). As a comparison, Hauglustaine et al. (2014) estimated a negative radiative forcing from nitrate under RCP8.5 of around  $-115 \text{ mW}\cdot\text{m}^{-2}$
- 585 (as pre-industrial emissions state as the baseline). These results from CAMEO[434-126] and CAMEO[434-370] suggest a significant impact of the future evolution of the  $\text{NH}_3$  emissions on the climate depending on the mitigation measures that would be undertaken for  $\text{NO}_x$  and  $\text{SO}_2$  emissions.
8. In addition to the aerosol radiative effect, the  $\text{N}_2\text{O}$  production from the oxidation of  $\text{NH}_3$  has been estimated to be non-negligible in the present-day ( $1 \text{ Tg}(\text{N}_2\text{O})\text{yr}^{-1}$ ) and could represent up to 18% ( $2.9 \text{ Tg}(\text{N}_2\text{O})\text{yr}^{-1}$ ) of the future
- 590  $\text{N}_2\text{O}$  anthropogenic emissions under our highest future  $\text{NO}_x$  scenario (SSP3-7.0). Even though agricultural production is one of the most significant sector which impacts the N cycle, the potential use of ammonia for low-carbon energy production is rising the attention. The emerging ammonia economy, linked to hydrogen fuel has been estimated to produce an additional  $\text{N}_2\text{O}$  emissions of  $1 \text{ Tg}(\text{N}_2\text{O})\text{yr}^{-1}$  when considering a high estimate of reactive N emissions from the ammonia use in the energy sector (Bertagni et al., 2023). Knowing that a 1% conversion of nitrogen in ammonia
- 595 into  $\text{N}_2\text{O}$  was used in the latter study, and that our estimate ranges between 1.5% and 2.25% depending on the scenario, we can expect a greater impact from the new global-scale ammonia economy.
9. In this paper, the set of simulations designed aimed at isolating the impact of emissions shift by keeping the meteorology at its present-day levels during 2090-2100. In a following study, additional simulations will be performed by changing the meteorology under future scenario and investigating the dual impact of emissions and climate change. In addition,
- 600 the N species exchanges (deposition and emissions) at the interface between the atmosphere and the surface are currently under development in the IPSL-ESM via an interactive coupling and similar impacts on the chemistry and climate will be analyzed in this new framework.

*Code availability.* The LMDZ-INCA global model is part of the Institut Pierre Simon Laplace (IPSL) Climate Modelling Center Coupled Model. The documentation on the code and the code itself can be found at <https://cmc.ipsl.fr/ipsclimate-models/ipsl-cm6/> (IPSL, 2024).

- 605 The Python scripts used for analysing the data and plotting the analysed data are available from the corresponding author upon reasonable request. The ammonia columns measured from the IASI instrument onto the LMDZ grid are also available from the corresponding author upon request.



*Data availability.* To access datasets of LMDZ-INCA results, please contact the corresponding author. Present-day and future simulated emissions from CAMEO can be respectively found at the following Zenodo repositories: <https://zenodo.org/records/6818373>, (Beaudor et al., 2022) and <https://doi.org/10.5281/zenodo.10100435>, (Beaudor et al., 2023b)

*Author contributions.* NV, DH, JL, and MB designed the study. DH and MB prepared the emission sets and the model configuration. MB performed the simulation experiments, analyzed the output and prepared the manuscript with contributions from NV, DH, and JL. MVD and LC provided the IASI satellite product and performed the regridding of the data. All of the authors contributed to writing the manuscript.

*Competing interests.* The authors declare that they have no conflict of interest.

615 *Acknowledgements.* This study was partly funded by the European Union Horizon 2020 research and innovation programme under the ESM2025 project (grant agreement no. 101003536) and by the the Research Council of Norway under project No. 336227 “AMMONIA: Climate and environmental impacts of green ammonia (NH<sub>3</sub>)”. The simulations were performed using HPC resources from GENCI (Grand Equipement National de Calcul Intensif) under project gen2201 and gen6328. Lieven Clarisse is a research associate supported by the Belgian F.R.S.-FNRS. We also thank Yao Ge for the open-access Python scripts exploited for evaluating the model to the ground-based observations.

620 We are grateful for the technical support received from Anne Cozic and the fruitful discussions with Fabien Paulot.

*Financial support.* This study was partly funded by the European Union Horizon 2020 research and innovation programme under the ESM2025 project (grant agreement no. 101003536) and by the the Research Council of Norway under project No. 336227 “AMMONIA: Climate and environmental impacts of green ammonia (NH<sub>3</sub>)”.



## References

- 625 Abbatt, J. P. D., Benz, S., Cziczo, D. J., Kanji, Z., Lohmann, U., and Möhler, O.: Solid Ammonium Sulfate Aerosols as Ice Nuclei: A Pathway for Cirrus Cloud Formation, *Science*, 313, 1770–1773, <https://doi.org/10.1126/science.1129726>, publisher: American Association for the Advancement of Science, 2006.
- Anderson, N., Strader, R., and Davidson, C.: Airborne reduced nitrogen: ammonia emissions from agriculture and other sources, *Environment International*, 29, 277–286, [https://doi.org/10.1016/S0160-4120\(02\)00186-1](https://doi.org/10.1016/S0160-4120(02)00186-1), 2003.
- 630 Bauer, S. E., Balkanski, Y., Schulz, M., Hauglustaine, D. A., and Dentener, F.: Global modeling of heterogeneous chemistry on mineral aerosol surfaces: Influence on tropospheric ozone chemistry and comparison to observations, *Journal of Geophysical Research: Atmospheres*, 109, <https://doi.org/10.1029/2003JD003868>, eprint: <https://onlinelibrary.wiley.com/doi/pdf/10.1029/2003JD003868>, 2004.
- Bauer, S. E., Koch, D., Unger, N., Metzger, S. M., Shindell, D. T., and Streets, D. G.: Nitrate aerosols today and in 2030: a global simulation including aerosols and tropospheric ozone, *Atmospheric Chemistry and Physics*, 7, 5043–5059, <https://doi.org/10.5194/acp-7-5043-2007>, publisher: Copernicus GmbH, 2007.
- 635 Beaudor, M., Vuichard, N., Lathière, J., Evangeliou, N., Van Damme, M., Clarisse, L., and Hauglustaine, D.: Global agricultural ammonia emissions simulated with the ORCHIDEE land surface model : Model Output Data [Dataset] Zenodo, <https://doi.org/10.5281/zenodo.6818373>, 2022.
- Beaudor, M., Vuichard, N., Lathière, J., Evangeliou, N., Van Damme, M., Clarisse, L., and Hauglustaine, D.: Global agricultural ammonia emissions simulated with the ORCHIDEE land surface model, *Geoscientific Model Development*, 16, 1053–1081, <https://doi.org/10.5194/gmd-16-1053-2023>, publisher: Copernicus GmbH, 2023a.
- 640 Beaudor, M., Vuichard, N., Lathière, J., and Hauglustaine, D.: Global ammonia emissions from CAMEO throughout the century for 3 scenarios (2000-2100) [Dataset] Zenodo, <https://doi.org/10.5281/zenodo.10100435>, 2023b.
- Beaudor, M., Vuichard, N., Lathière, J., and Hauglustaine, D.: Future trends of agricultural ammonia global emissions in a changing climate, <https://doi.org/10.22541/essoar.170542263.35872590/v1>, 2024.
- 645 Behera, S. N., Sharma, M., Aneja, V. P., and Balasubramanian, R.: Ammonia in the atmosphere: a review on emission sources, atmospheric chemistry and deposition on terrestrial bodies, *Environmental Science and Pollution Research*, 20, 8092–8131, <https://doi.org/10.1007/s11356-013-2051-9>, 2013.
- Bertagni, M. B., Socolow, R. H., Martirez, J. M. P., Carter, E. A., Greig, C., Ju, Y., Lieuwen, T., Mueller, M. E., Sundaresan, S., Wang, R., Zondlo, M. A., and Porporato, A.: Minimizing the impacts of the ammonia economy on the nitrogen cycle and climate, *Proceedings of the National Academy of Sciences*, 120, e2311728 120, <https://doi.org/10.1073/pnas.2311728120>, publisher: Proceedings of the National Academy of Sciences, 2023.
- 650 Bian, H., Chin, M., Hauglustaine, D. A., Schulz, M., Myhre, G., Bauer, S. E., Lund, M. T., Karydis, V. A., Kucsera, T. L., Pan, X., Pozzer, A., Skeie, R. B., Steenrod, S. D., Sudo, K., Tsigaridis, K., Tsimpidi, A. P., and Tsyro, S. G.: Investigation of global particulate nitrate from the AeroCom phase III experiment, *Atmospheric Chemistry and Physics*, 17, 12911–12940, <https://doi.org/10.5194/acp-17-12911-2017>, 2017.
- 655 Boucher, O., Servonnat, J., Albright, A. L., Aumont, O., Balkanski, Y., Bastrikov, V., Bekki, S., Bonnet, R., Bony, S., Bopp, L., Braconnot, P., Brockmann, P., Cadule, P., Caubel, A., Cheruy, F., Codron, F., Cozic, A., Cugnet, D., D’Andrea, F., Davini, P., de Lavergne, C., Denvil, S., Deshayes, J., Devilliers, M., Ducharne, A., Dufresne, J.-L., Dupont, E., Éthé, C., Fairhead, L., Falletti, L., Flavoni, S., Foujols, M.-A., Gardoll, S., Gastineau, G., Ghattas, J., Grandpeix, J.-Y., Guenet, B., Guez, Lionel, E., Guilyardi, E., Guimberteau, M., Hauglustaine, D.,



- Hourdin, F., Idelkadi, A., Joussaume, S., Kageyama, M., Khodri, M., Krinner, G., Lebas, N., Levavasseur, G., Lévy, C., Li, L., Lott, F., Lurton, T., Luysaert, S., Madec, G., Madeleine, J.-B., Maignan, F., Marchand, M., Marti, O., Mellul, L., Meurdesoif, Y., Mignot, J., Musat, I., Ottlé, C., Peylin, P., Planton, Y., Polcher, J., Rio, C., Rochetin, N., Rousset, C., Sepulchre, P., Sima, A., Swingedouw, D., Thiéblemont, R., Traore, A. K., Vancoppenolle, M., Vial, J., Vialard, J., Viovy, N., and Vuichard, N.: Presentation and Evaluation of the IPSL-CM6A-LR Climate Model, *Journal of Advances in Modeling Earth Systems*, 12, e2019MS002 010, <https://doi.org/10.1029/2019MS002010>, <https://onlinelibrary.wiley.com/doi/pdf/10.1029/2019MS002010>, 2020.
- 665 Bouwman, A. F., Lee, D. S., Asman, W. a. H., Dentener, F. J., Van Der Hoek, K. W., and Olivier, J. G. J.: A global high-resolution emission inventory for ammonia, *Global Biogeochemical Cycles*, 11, 561–587, <https://doi.org/10.1029/97GB02266>, 1997.
- Clarisse, L., Shephard, M. W., Dentener, F., Hurtmans, D., Cady-Pereira, K., Karagulian, F., Van Damme, M., Clerbaux, C., and Coheur, P.-F.: Satellite monitoring of ammonia: A case study of the San Joaquin Valley, *Journal of Geophysical Research: Atmospheres*, 115, D13 302, <https://doi.org/10.1029/2009JD013291>, publisher: American Geophysical Union, 2010.
- 670 Crippa, M., Solazzo, E., Huang, G., Guizzardi, D., Koffi, E., Muntean, M., Schieberle, C., Friedrich, R., and Janssens-Maenhout, G.: High resolution temporal profiles in the Emissions Database for Global Atmospheric Research, *Scientific Data*, 7, 121, <https://doi.org/10.1038/s41597-020-0462-2>, number: 1 Publisher: Nature Publishing Group, 2020.
- 675 de Vries, W.: Impacts of nitrogen emissions on ecosystems and human health: A mini review, *Current Opinion in Environmental Science & Health*, 21, 100 249, <https://doi.org/10.1016/j.coesh.2021.100249>, 2021.
- Dentener, F. J. and Crutzen, P. J.: A three-dimensional model of the global ammonia cycle, *Journal of Atmospheric Chemistry*, 19, 331–369, <https://doi.org/10.1007/BF00694492>, 1994.
- Evangelioiu, N., Balkanski, Y., Eckhardt, S., Cozic, A., Damme, V., Coheur, P.-F., Clarisse, L., Shephard, M. W., Cady-Pereira, K. E., and Hauglustaine, D.: 1 10–year satellite–constrained fluxes of ammonia improve 2 performance of chemistry transport models, p. 41, 2020.
- 680 Eyring, V., Lamarque, J.-F., Hess, P., Arfeuille, F., Bowman, K., Chipperfield, M., Duncan, B., Fiore, A., Gettelman, A., Giorgetta, M., Granier, C., Heggin, M., Kinnison, D., Kunze, M., Langematz, U., Luo, B., Martin, R., Matthes, K., Newman, P., and Young, P.: Overview of IGAC/SPARC Chemistry-Climate Model Initiative (CCMI) community simulations in support of upcoming ozone and climate assessments, 40, 48–66, 2013.
- 685 Folberth, G. A., Hauglustaine, D. A., Lathière, J., and Brocheton, F.: Interactive chemistry in the Laboratoire de Météorologie Dynamique general circulation model: model description and impact analysis of biogenic hydrocarbons on tropospheric chemistry, *Atmospheric Chemistry and Physics*, 6, 2273–2319, <https://doi.org/10.5194/acp-6-2273-2006>, 2006.
- Ge, X., Schaap, M., Kranenburg, R., Segers, A., Reinds, G. J., Kros, H., and de Vries, W.: Modeling atmospheric ammonia using agricultural emissions with improved spatial variability and temporal dynamics, *Atmospheric Chemistry and Physics*, 20, 16 055–16 087, <https://doi.org/10.5194/acp-20-16055-2020>, publisher: Copernicus GmbH, 2020.
- 690 Ge, Y., Heal, M. R., Stevenson, D. S., Wind, P., and Vieno, M.: Evaluation of global EMEP MSC-W (rv4.34) WRF (v3.9.1.1) model surface concentrations and wet deposition of reactive N and S with measurements, *Geoscientific Model Development*, 14, 7021–7046, <https://doi.org/10.5194/gmd-14-7021-2021>, 2021.
- Ge, Y., Vieno, M., Stevenson, D., Wind, P., and Heal, M.: A new assessment of global and regional budgets, fluxes and lifetimes of atmospheric reactive N and S gases and aerosols, preprint, *Aerosols/Atmospheric Modelling/Troposphere/Chemistry (chemical composition and reactions)*, <https://doi.org/10.5194/acp-2022-82>, 2022.
- 695



- Gidden, M. J., Fujimori, S., van den Berg, M., Klein, D., Smith, S. J., van Vuuren, D. P., and Riahi, K.: A methodology and implementation of automated emissions harmonization for use in Integrated Assessment Models, *Environmental Modelling & Software*, 105, 187–200, <https://doi.org/10.1016/j.envsoft.2018.04.002>, 2018.
- 700 Gliß, J., Mortier, A., Schulz, M., Andrews, E., Balkanski, Y., Bauer, S. E., Benedictow, A. M. K., Bian, H., Checa-Garcia, R., Chin, M., Ginoux, P., Griesfeller, J. J., Heckel, A., Kipling, Z., Kirkevåg, A., Kokkola, H., Laj, P., Le Sager, P., Lund, M. T., Lund Myhre, C., Matsui, H., Myhre, G., Neubauer, D., van Noije, T., North, P., Olivié, D. J. L., Rémy, S., Sogacheva, L., Takemura, T., Tsigaridis, K., and Tsyro, S. G.: AeroCom phase III multi-model evaluation of the aerosol life cycle and optical properties using ground- and space-based remote sensing as well as surface in situ observations, *Atmospheric Chemistry and Physics*, 21, 87–128, [https://doi.org/10.5194/acp-21-](https://doi.org/10.5194/acp-21-87-2021)  
705 87-2021, publisher: Copernicus GmbH, 2021.
- Guo, X., Wang, R., Pan, D., Zondlo, M. A., Clarisse, L., Van Damme, M., Whitburn, S., Coheur, P.-F., Clerbaux, C., Franco, B., Golston, L. M., Wendt, L., Sun, K., Tao, L., Miller, D., Mikoviny, T., Müller, M., Wisthaler, A., Tevlin, A. G., Murphy, J. G., Nowak, J. B., Roscioli, J. R., Volkamer, R., Kille, N., Neuman, J. A., Eilerman, S. J., Crawford, J. H., Yacovitch, T. I., Barrick, J. D., and Scarino, A. J.: Validation of IASI Satellite Ammonia Observations at the Pixel Scale Using In Situ Vertical Profiles, *Journal of Geophysical Research: Atmospheres*, 126, e2020JD033475, <https://doi.org/10.1029/2020JD033475>, \_eprint: <https://onlinelibrary.wiley.com/doi/pdf/10.1029/2020JD033475>,  
710 2021.
- Guthrie, S., Giles, S., Dunkerley, F., Tabaqchali, H., Harshfield, A., Ioppolo, B., and Manville, C.: Impact of ammonia emissions from agriculture on biodiversity: An evidence synthesis, Tech. rep., RAND Corporation, [https://www.rand.org/pubs/research\\_reports/RR2695.html](https://www.rand.org/pubs/research_reports/RR2695.html), 2018.
- 715 Hauglustaine, D. A., Hourdin, F., Jourdain, L., Filiberti, M.-A., Walters, S., Lamarque, J.-F., and Holland, E. A.: Interactive chemistry in the Laboratoire de Météorologie Dynamique general circulation model: Description and background tropospheric chemistry evaluation, *Journal of Geophysical Research: Atmospheres*, 109, <https://doi.org/10.1029/2003JD003957>, 2004.
- Hauglustaine, D. A., Balkanski, Y., and Schulz, M.: A global model simulation of present and future nitrate aerosols and their direct radiative forcing of climate, *Atmospheric Chemistry and Physics*, 14, 11 031–11 063, <https://doi.org/10.5194/acp-14-11031-2014>, publisher:  
720 Copernicus GmbH, 2014.
- Heald, C. L., Jr, J. L. C., Lee, T., Benedict, K. B., Schwandner, F. M., Li, Y., Clarisse, L., and Hurtmans, D. R.: Atmospheric ammonia and particulate inorganic nitrogen over the United States, *Atmos. Chem. Phys.*, p. 19, 2012.
- Henze, D. K., Shindell, D. T., Akhtar, F., Spurr, R. J. D., Pinder, R. W., Loughlin, D., Kopacz, M., Singh, K., and Shim, C.: Spatially Refined Aerosol Direct Radiative Forcing Efficiencies, *Environmental Science & Technology*, 46, 9511–9518, <https://doi.org/10.1021/es301993s>,  
725 publisher: American Chemical Society, 2012.
- Hoesly, R. M., Smith, S. J., Feng, L., Klimont, Z., Janssens-Maenhout, G., Pitkanen, T., Seibert, J. J., Vu, L., Andres, R. J., Bolt, R. M., Bond, T. C., Dawidowski, L., Kholod, N., Kurokawa, J.-i., Li, M., Liu, L., Lu, Z., Moura, M. C. P., O'Rourke, P. R., and Zhang, Q.: Historical (1750–2014) anthropogenic emissions of reactive gases and aerosols from the Community Emissions Data System (CEDS), *Geoscientific Model Development*, 11, 369–408, <https://doi.org/10.5194/gmd-11-369-2018>, publisher: Copernicus GmbH, 2018.
- 730 Hourdin, F., Rio, C., Grandpeix, J.-Y., Madeleine, J.-B., Cheruy, F., Rochetin, N., Jam, A., Musat, I., Idelkadi, A., Fairhead, L., Foujols, M.-A., Mellul, L., Traore, A.-K., Dufresne, J.-L., Boucher, O., Lefebvre, M.-P., Millour, E., Vignon, E., Jouhaud, J., Diallo, F. B., Lott, F., Gastineau, G., Caubel, A., Meurdesoif, Y., and Ghattas, J.: LMDZ6A: The Atmospheric Component of the IPSL Climate Model With Improved and Better Tuned Physics, *Journal of Advances in Modeling Earth Systems*, 12, e2019MS001892, <https://doi.org/10.1029/2019MS001892>, 2020.



- 735 Intergovernmental Panel On Climate Change: Climate Change 2021 – The Physical Science Basis: Working Group I Contribution to the Sixth Assessment Report of the Intergovernmental Panel on Climate Change, Cambridge University Press, 1 edn., <https://doi.org/10.1017/9781009157896>, 2023.
- IPSL: IPSL Climate Models – My CMS, <https://cmc.ipsl.fr/ipsl-climate-models/>, 2024.
- Kohlmann, J.-P. and Poppe, D.: The Tropospheric Gas-Phase Degradation of NH<sub>3</sub> and Its Impact on the Formation of N<sub>2</sub>O and NO<sub>x</sub>, *Journal of Atmospheric Chemistry*, 32, 397–415, <https://doi.org/10.1023/A:1006162910279>, 1999.
- 740 Krinner, G., Viovy, N., Noblet-Ducoudré, N. d., Ogée, J., Polcher, J., Friedlingstein, P., Ciais, P., Sitch, S., and Prentice, I. C.: A dynamic global vegetation model for studies of the coupled atmosphere-biosphere system, *Global Biogeochemical Cycles*, 19, <https://doi.org/10.1029/2003GB002199>, 2005.
- Lachatre, M., Fortems-Cheiney, A., Foret, G., Siour, G., Dufour, G., Clarisse, L., Clerbaux, C., Coheur, P.-F., Van Damme, M., and Beekmann, M.: The unintended consequence of SO<sub>2</sub> and NO<sub>2</sub> regulations over China: increase of ammonia levels and impact on PM<sub>2.5</sub> concentrations, *Atmospheric Chemistry and Physics*, 19, 6701–6716, <https://doi.org/10.5194/acp-19-6701-2019>, 2019.
- 745 Lachatre, M., Foret, G., Laurent, B., Siour, G., Cuesta, J., Dufour, G., Meng, F., Tang, W., Zhang, Q., and Beekmann, M.: Air Quality Degradation by Mineral Dust over Beijing, Chengdu and Shanghai Chinese Megacities, *Atmosphere*, 11, 708, <https://doi.org/10.3390/atmos11070708>, 2020.
- 750 Lamarque, J.-F., Bond, T. C., Eyring, V., Granier, C., Heil, A., Klimont, Z., Lee, D., Lioussé, C., Mieville, A., Owen, B., Schultz, M. G., Shindell, D., Smith, S. J., Stehfest, E., Van Aardenne, J., Cooper, O. R., Kainuma, M., Mahowald, N., McConnell, J. R., Naik, V., Riahi, K., and van Vuuren, D. P.: Historical (1850–2000) gridded anthropogenic and biomass burning emissions of reactive gases and aerosols: methodology and application, *Atmospheric Chemistry and Physics*, 10, 7017–7039, <https://doi.org/10.5194/acp-10-7017-2010>, publisher: Copernicus GmbH, 2010.
- 755 Liu, L., Xu, W., Lu, X., Zhong, B., Guo, Y., Lu, X., Zhao, Y., He, W., Wang, S., Zhang, X., Liu, X., and Vitousek, P.: Exploring global changes in agricultural ammonia emissions and their contribution to nitrogen deposition since 1980, *Proceedings of the National Academy of Sciences*, 119, e2121998 119, <https://doi.org/10.1073/pnas.2121998119>, publisher: Proceedings of the National Academy of Sciences, 2022.
- 760 McDuffie, E. E., Smith, S. J., O'Rourke, P., Tibrewal, K., Venkataraman, C., Marais, E. A., Zheng, B., Crippa, M., Brauer, M., and Martin, R. V.: A global anthropogenic emission inventory of atmospheric pollutants from sector- and fuel-specific sources (1970–2017): an application of the Community Emissions Data System (CEDs), *Earth System Science Data*, 12, 3413–3442, <https://doi.org/10.5194/essd-12-3413-2020>, publisher: Copernicus GmbH, 2020.
- Messina, P., Lathière, J., Sindelarova, K., Vuichard, N., Granier, C., Ghattas, J., Cozic, A., and Hauglustaine, D. A.: Global biogenic volatile organic compound emissions in the ORCHIDEE and MEGAN models and sensitivity to key parameters, *Atmospheric Chemistry and Physics*, 16, 14 169–14 202, <https://doi.org/10.5194/acp-16-14169-2016>, publisher: Copernicus GmbH, 2016.
- 765 Metzger, S., Dentener, F., Pandis, S., and Lelieveld, J.: Gas/aerosol partitioning: 1. A computationally efficient model, *Journal of Geophysical Research: Atmospheres*, 107, ACH 16–1–ACH 16–24, <https://doi.org/10.1029/2001JD001102>, <https://onlinelibrary.wiley.com/doi/pdf/10.1029/2001JD001102>, 2002.
- 770 O'Neill, B. C., Tebaldi, C., van Vuuren, D. P., Eyring, V., Friedlingstein, P., Hurtt, G., Knutti, R., Kriegler, E., Lamarque, J.-F., Lowe, J., Meehl, G. A., Moss, R., Riahi, K., and Sanderson, B. M.: The Scenario Model Intercomparison Project (ScenarioMIP) for CMIP6, *Geoscientific Model Development*, 9, 3461–3482, <https://doi.org/10.5194/gmd-9-3461-2016>, 2016.





- Pai, S. J., Heald, C. L., and Murphy, J. G.: Exploring the Global Importance of Atmospheric Ammonia Oxidation, *ACS Earth and Space Chemistry*, 5, 1674–1685, <https://doi.org/10.1021/acsearthspacechem.1c00021>, 2021.
- 775 Paulot, F., Ginoux, P., Cooke, W. F., Donner, L. J., Fan, S., Lin, M.-Y., Mao, J., Naik, V., and Horowitz, L. W.: Sensitivity of nitrate aerosols to ammonia emissions and to nitrate chemistry: implications for present and future nitrate optical depth, *Atmospheric Chemistry and Physics*, 16, 1459–1477, <https://doi.org/10.5194/acp-16-1459-2016>, 2016.
- Pleim, J. E., Ran, L., Appel, W., Shephard, M. W., and Cady-Pereira, K.: New Bidirectional Ammonia Flux Model in an Air Quality Model Coupled With an Agricultural Model, *Journal of advances in modeling earth systems*, 11, 2934–2957, <https://doi.org/10.1029/2019MS001728>, 2019.
- 780 Ren, C., Huang, X., Liu, T., Song, Y., Wen, Z., Liu, X., Ding, A., and Zhu, T.: A dynamic ammonia emission model and the online coupling with WRF–Chem (WRF–SoilN–Chem v1.0): development and regional evaluation in China, *Geoscientific Model Development*, 16, 1641–1659, <https://doi.org/10.5194/gmd-16-1641-2023>, publisher: Copernicus GmbH, 2023.
- Sander, R.: Compilation of Henry’s law constants (version 4.0) for water as solvent, *Atmospheric Chemistry and Physics*, 15, 4399–4981, <https://doi.org/10.5194/acp-15-4399-2015>, 2015.
- 785 Schulz, M.: Constraining model estimates of the aerosol radiative forcing, Université Pierre et Marie Curie, Paris VI, Paris, 2007.
- Simpson, D., Benedictow, A., Berge, H., Bergström, R., Emberson, L. D., Fagerli, H., Flechard, C. R., Hayman, G. D., Gauss, M., Jonson, J. E., Jenkin, M. E., Nyíri, A., Richter, C., Semeena, V. S., Tsyro, S., Tuovinen, J.-P., Valdebenito, , and Wind, P.: The EMEP MSC-W chemical transport model &ndash; technical description, *Atmospheric Chemistry and Physics*, 12, 7825–7865, <https://doi.org/10.5194/acp-12-7825-2012>, publisher: Copernicus GmbH, 2012.
- 790 Stevens, C. J., Bell, J. N. B., Brimblecombe, P., Clark, C. M., Dise, N. B., Fowler, D., Lovett, G. M., and Wolesey, P. A.: The impact of air pollution on terrestrial managed and natural vegetation, *Philosophical Transactions of the Royal Society A: Mathematical, Physical and Engineering Sciences*, 378, 20190 317, <https://doi.org/10.1098/rsta.2019.0317>, publisher: Royal Society, 2020.
- Sutton, M. A., Nemitz, E., Erisman, J. W., Beier, C., Bahl, K. B., Cellier, P., de Vries, W., Cotrufo, F., Skiba, U., Di Marco, C., Jones, S., Laville, P., Soussana, J. F., Loubet, B., Twigg, M., Famulari, D., Whitehead, J., Gallagher, M. W., Neftel, A., Flechard, C. R., Her-  
795 rmann, B., Calanca, P. L., Schjoerring, J. K., Daemmgen, U., Horvath, L., Tang, Y. S., Emmett, B. A., Tietema, A., Peñuelas, J., Kesik, M., Brüeggemann, N., Pilegaard, K., Vesala, T., Campbell, C. L., Olesen, J. E., Dragosits, U., Theobald, M. R., Levy, P., Mobbs, D. C., Milne, R., Viovy, N., Vuichard, N., Smith, J. U., Smith, P., Bergamaschi, P., Fowler, D., and Reis, S.: Challenges in quantifying biosphere–atmosphere exchange of nitrogen species, *Environmental Pollution*, 150, 125–139, <https://doi.org/10.1016/j.envpol.2007.04.014>, 2007.
- 800 Taylor, K. E.: Summarizing multiple aspects of model performance in a single diagram, *Journal of Geophysical Research: Atmospheres*, 106, 7183–7192, <https://doi.org/10.1029/2000JD900719>, \_eprint: <https://onlinelibrary.wiley.com/doi/pdf/10.1029/2000JD900719>, 2001.
- Tian, H., Pan, N., Thompson, R. L., Canadell, J. G., Suntharalingam, P., Regnier, P., Davidson, E. A., Prather, M., Ciais, P., Muntean, M., Pan, S., Winiwarter, W., Zaehle, S., Zhou, F., Jackson, R. B., Bange, H. W., Berthet, S., Bian, Z., Bianchi, D., Bouwman, A. F., Buitenhuis, E. T., Dutton, G., Hu, M., Ito, A., Jain, A. K., Jeltsch-Thömmes, A., Joos, F., Kou-Giesbrecht, S., Krummel, P. B., Lan, X., Landolfi, A., Lauerwald, R., Li, Y., Lu, C., Maavara, T., Manizza, M., Millet, D. B., Mühle, J., Patra, P. K., Peters, G. P., Qin, X., Raymond, P.,  
805 Resplandy, L., Rosentreter, J. A., Shi, H., Sun, Q., Tonina, D., Tubiello, F. N., van der Werf, G. R., Vuichard, N., Wang, J., Wells, K. C., Western, L. M., Wilson, C., Yang, J., Yao, Y., You, Y., and Zhu, Q.: Global nitrous oxide budget (1980–2020), *Earth System Science Data*, 16, 2543–2604, <https://doi.org/10.5194/essd-16-2543-2024>, publisher: Copernicus GmbH, 2024.



- 810 Van Damme, M., Wichink Kruit, R. J., Schaap, M., Clarisse, L., Clerbaux, C., Coheur, P.-F., Dammers, E., Dolman, A. J., and Erisman, J. W.: Evaluating 4 years of atmospheric ammonia (NH<sub>3</sub>) over Europe using IASI satellite observations and LOTOS-EUROS model results, *Journal of Geophysical Research: Atmospheres*, 119, 9549–9566, <https://doi.org/10.1002/2014JD021911>, 2014.
- Van Damme, M., Whitburn, S., Clarisse, L., Clerbaux, C., Hurtmans, D., and Coheur, P.-F.: Version 2 of the IASI NH<sub>3</sub> neural network retrieval algorithm: near-real-time and reanalysed datasets, *Atmospheric Measurement Techniques*, 10, 4905–4914, <https://doi.org/10.5194/amt-10-4905-2017>, publisher: Copernicus GmbH, 2017.
- 815 Van Damme, M., Clarisse, L., Franco, B., Sutton, M. A., Erisman, J. W., Wichink Kruit, R., van Zanten, M., Whitburn, S., Hadji-Lazaro, J., Hurtmans, D., Clerbaux, C., and Coheur, P.-F.: Global, regional and national trends of atmospheric ammonia derived from a decadal (2008–2018) satellite record, *Environmental Research Letters*, 16, 055 017, <https://doi.org/10.1088/1748-9326/abd5e0>, 2021.
- Vira, J., Hess, P., Melkonian, J., and Wieder, W. R.: An improved mechanistic model for ammonia volatilization in Earth system models: Flow of Agricultural Nitrogen, version 2 (FANv2), *Geoscientific Model Development Discussions*, pp. 1–49, <https://doi.org/10.5194/gmd-2019-233>, 2019.
- 820 Vira, J., Hess, P., Ossohou, M., and Galy-Lacaux, C.: Evaluation of interactive and prescribed agricultural ammonia emissions for simulating atmospheric composition in CAM-chem, *Atmospheric Chemistry and Physics*, 22, 1883–1904, <https://doi.org/10.5194/acp-22-1883-2022>, 2022.
- Vuichard, N., Messina, P., Luyssaert, S., Guenet, B., Zaehle, S., Ghattas, J., Bastrikov, V., and Peylin, P.: Accounting for carbon and nitrogen interactions in the global terrestrial ecosystem model ORCHIDEE (trunk version, rev 4999): multi-scale evaluation of gross primary production, *Geoscientific Model Development*, 12, 4751–4779, <https://doi.org/10.5194/gmd-12-4751-2019>, publisher: Copernicus GmbH, 2019.
- 825 Wang, R., Guo, X., Pan, D., Kelly, J. T., Bash, J. O., Sun, K., Paulot, F., Clarisse, L., Van Damme, M., Whitburn, S., Coheur, P.-F., Clerbaux, C., and Zondlo, M. A.: Monthly Patterns of Ammonia Over the Contiguous United States at 2-km Resolution, *Geophysical Research Letters*, 48, e2020GL090 579, <https://doi.org/10.1029/2020GL090579>, <https://onlinelibrary.wiley.com/doi/pdf/10.1029/2020GL090579>, 2021.
- Whitburn, S., Damme, M. V., Clarisse, L., Bauduin, S., Heald, C. L., Hadji-Lazaro, J., Hurtmans, D., Zondlo, M. A., Clerbaux, C., and Coheur, P.-F.: A flexible and robust neural network IASI-NH<sub>3</sub> retrieval algorithm, *Journal of Geophysical Research: Atmospheres*, 121, 6581–6599, <https://doi.org/10.1002/2016JD024828>, 2016.
- 835 Xu, L. and Penner, J. E.: Global simulations of nitrate and ammonium aerosols and their radiative effects, *Atmospheric Chemistry and Physics*, 12, 9479–9504, <https://doi.org/10.5194/acp-12-9479-2012>, 2012.
- Xu, W., Zhang, L., and Liu, X.: A database of atmospheric nitrogen concentration and deposition from the nationwide monitoring network in China, *Scientific Data*, 6, 51, <https://doi.org/10.1038/s41597-019-0061-2>, number: 1 Publisher: Nature Publishing Group, 2019.